

The Relationship Between Crack-Tip Strain and Subcritical Cracking Thresholds for Steels in High-Pressure Hydrogen Gas

KEVIN A. NIBUR, BRIAN P. SOMERDAY, CHRIS SAN MARCHI,
JAMES W. FOULK, III, MOHSEN DADFARNIA, and PETROS SOFRONIS

Threshold stress intensity factors were measured in high-pressure hydrogen gas for a variety of low alloy ferritic steels using both constant crack opening displacement and rising crack opening displacement procedures. Thresholds for crack extension under rising displacement, K_{THi} , for crack extension under constant displacement, K_{THa}^* , and for crack arrest under constant displacement K_{THa} , were identified. These values were not found to be equivalent, *i.e.* $K_{THi} < K_{THa} < K_{THi}^*$. The hydrogen assisted fracture mechanism was determined to be strain controlled for all of the alloys in this study, and the micromechanics of strain controlled fracture are used to explain the observed disparities between the different threshold measurements. K_{THa} and K_{THi} differ because the strain singularity of a stationary crack is stronger than that of a propagating crack; K_{THa} must be larger than K_{THi} to achieve equivalent crack tip strain at the same distance from the crack tip. Hydrogen interacts with deformation mechanisms, enhancing strain localization and consequently altering both the nucleation and growth stages of strain controlled fracture mechanisms. The timing of load application and hydrogen exposure, *i.e.*, sequential for constant displacement tests and concurrent for rising displacement tests, leads to differences in the strain history relative to the environmental exposure history and promotes the disparity between K_{THi}^* and K_{THi} . K_{THi} is the only conservative measurement of fracture threshold among the methods presented here.

DOI: 10.1007/s11661-012-1400-5

© The Minerals, Metals & Materials Society and ASM International 2012

I. INTRODUCTION

HYDROGEN reduces the fracture resistance (*e.g.*, promotes subcritical cracking) in most structural metals, as documented over many decades, *e.g.*^[1–9] Implementation of a fracture mechanics-based design qualification approach for hydrogen containment and transport components could greatly enhance life prediction, reducing the probability for catastrophic failures associated with subcritical crack propagation. Reliable and appropriately conservative subcritical cracking thresholds measured under quasi-static loading in high-pressure

hydrogen gas are necessary inputs to effective fracture mechanics-based life prediction assessments. As the range of applications and performance requirements for high-pressure hydrogen containment structures expands beyond the current technology space, fracture mechanics-based design approaches and methods for measuring subcritical cracking thresholds in hydrogen gas become increasingly important to enhance safety.

Laboratory test methods for measuring subcritical cracking thresholds in hydrogen gas must properly simulate the in-service mechanical and environmental conditions of components, *i.e.*, the concept of similitude must be considered for both the mechanical and environmental conditions at the crack tip.^[10] Mechanical similitude may be maintained through the use of standard fracture mechanics methods designed to measure the linear-elastic stress intensity factor, K , or the elastic-plastic J -integral, J . These fracture mechanics parameters provide a relationship between the continuum crack-tip fields and the remote loading conditions, and this relationship is not a function of the environment, especially for low hydrogen solubility systems such as ferritic steel. Mechanical similitude is dictated predominantly by the geometry and remote loading conditions of the laboratory specimen and service component, independent of environment. Maintaining similitude in the crack-tip hydrogen environment between the laboratory specimen and service component is more challenging. One method to achieve environmental similitude is to replicate the service environment during laboratory testing; in this study, high-pressure hydrogen gas is used to enable environmental similitude.

KEVIN A. NIBUR, Researcher and Owner, is with Hy-Performance Materials Testing, LLC, Bend, OR. Contact e-mail: Kevin@hy-performancetesting.com BRIAN P. SOMERDAY, Distinguished Member of Technical Staff, is with Hydrogen and Metallurgy Science Department, Sandia National Laboratories, P.O. Box 969, Livermore, CA 94551, and also with International Institute for Carbon Neutral Energy Research (WPI-I2CNER), Kyushu University, 744 Moto-oka, Nishi-ku, Fukuoka 819-0395, Japan. CHRIS SAN MARCHI, Principal Member of Technical Staff, is with Hydrogen and Metallurgy Science Department, Sandia National Laboratories. JAMES W. FOULK, III, Principal Member of Technical Staff, is with Mechanics of Materials Department, Sandia National Laboratories. MOHSEN DADFARNIA, Research Associate, is with the Department of Mechanical Science and Engineering, University of Illinois at Urbana-Champaign, 1206 West Green St., Urbana, Illinois 61801, and also with International Institute for Carbon Neutral Energy Research (WPI-I2CNER), Kyushu University. PETROS SOFRONIS, Professor, is with the Department of Mechanical Science and Engineering, University of Illinois at Urbana-Champaign, and also, Director, with International Institute for Carbon Neutral Energy Research (WPI-I2CNER), Kyushu University.

Manuscript submitted March 5, 2012.

Article published online November 7, 2012

Hydrogen-assisted cracking is a form of environment-assisted cracking (EAC). EAC broadly refers to any interaction between a metal and the external environment which facilitates time-dependent, subcritical cracking. Due to the time-dependent nature of the reactions that must occur between the metal and the environment, all forms of EAC are sensitive to variables that affect or preempt these kinetics, such as the applied loading rate. If the loading rate is such that crack extension outpaces hydrogen uptake and transport from the external environment to the crack-tip process zone, the effect of hydrogen on crack growth is diminished. For example, a study by Clark and Landes compared subcritical cracking threshold measurements from fixed-displacement and rising-load testing methods using high-strength (1100 to 1240 MPa yield strength) 4340 steel.^[11] A strong dependency on loading rate was observed in the rising-load experiments in hydrogen gas; subcritical cracking thresholds increased as loading rate increased. At very slow loading rates, the rising-load thresholds approached those from the fixed-displacement tests, suggesting that these latter thresholds were conservative for the high-strength steels employed in that study. These results are consistent with published efforts to model the kinetics of hydrogen assisted crack growth which generally consider hydrogen diffusion to the crack-tip process zone to be a rate limiting factor, *e.g.*^[12] For this reason, as well as the greater simplicity of conducting static-loading tests, many of the test methods that have been developed for measuring environment-assisted cracking thresholds, K_{IEAC} , employ constant load or constant displacement, such as those outlined in ASTM Standard E1681.^[13]

Constant-displacement tests have been used extensively and yield consistent and reliable results when applied to high-strength steels with relatively low subcritical cracking thresholds, *e.g.*^[14] They are described in materials testing standards, such as ASTM E1681. The initial proposal by Underwood *et al.*^[15] for including the constant-displacement method in ASTM E1681 was based largely on data from high-strength steels and nickel alloys (~1000 to 1400 MPa yield strength) in aqueous environments.^[16] The threshold stress-intensity factor at crack arrest in these steels was between 10 and 30 MPa \sqrt{m} .

The success and popularity of measuring subcritical cracking thresholds for high-strength steels using constant-displacement test methods has provided general confidence in this test method, yet the consequences of applying it to lower-strength steels have not been thoroughly explored. There are reports of non-conservative results from these types of tests when applied to low-to-intermediate strength steels with relatively high subcritical cracking thresholds.^[1,17,18,20] In one case, Gangloff reported that subcritical cracking thresholds measured for lower-strength steels under constant displacement were as much as four times higher than the thresholds measured under rising displacement,^[1] and the difference in threshold values diminished as the steel yield strength

increased up to about 1000 MPa. Mechanistic explanations for why constant-displacement tests may yield non-conservative thresholds for lower-strength steels have not been proposed.

The objective of this study is to rigorously measure rising-displacement and constant-displacement hydrogen-assisted cracking thresholds, K_{TH} , for low-to-intermediate strength steels in high-pressure hydrogen gas and to interpret results from the two methods in a crack-tip mechanics framework. Testing was conducted in 103 MPa (15,000 psi) hydrogen gas, since this pressure is generally viewed as the upper limit for compressed hydrogen storage and delivery in a hydrogen fuel infrastructure. A variety of pressure vessel steels was tested with emphasis on lower-strength steels that are technologically relevant to hydrogen storage and delivery components. Steels with ultimate tensile strengths less than 950 MPa are of particular interest since higher-strength steels are generally considered incompatible with high-pressure hydrogen gas.^[19] The effects of the initial applied stress-intensity factor, loading environment, and loading method (constant displacement *vs* rising displacement) are explored. Three definitions of the subcritical cracking threshold, K_{TH} , are evaluated, including crack-initiation and crack-arrest thresholds from constant-displacement tests as well as crack-initiation threshold from rising-displacement tests. Detailed data from this testing are presented in a previous report^[20]; the emphasis here is the mechanistic interpretation of the threshold measurements.

Three observations presented in the following sections are essential for developing the mechanistic framework: (1) subcritical cracking of low-to-intermediate strength steels in hydrogen gas is strain controlled, (2) subcritical cracking thresholds are higher when mechanical loading and hydrogen exposure are sequential relative to thresholds measured when loading and hydrogen exposure are concurrent, and (3) rising-displacement thresholds measured at the onset of subcritical cracking from a stationary crack are lower than constant-displacement thresholds measured from the arrest of propagating subcritical cracks. The first observation, *i.e.*, strain-controlled fracture, implies that the latter two observations of subcritical cracking behavior involve relatively complex crack-tip mechanics. In comparison, the subcritical cracking micromechanics associated with stress-controlled fracture (*e.g.*, intergranular fracture) are expected to lead to more consistent subcritical cracking trends, *i.e.*, thresholds measured from initiation at a stationary crack (rising-displacement test) and from arrest of a propagating crack (constant-displacement test) are not expected to vary significantly. This characteristic of stress-controlled fracture is related to the similarity in the tensile stress ahead of a propagating crack relative to that ahead of a stationary crack.^[21,22] The prominent difference in the stress fields for these two scenarios is the existence of a region of unloading behind the propagating crack tip. This crack-wake unloading has a negligible effect on the maximum tensile stress directly ahead of a crack tip, which is expected to govern stress-

controlled fracture, however it has significant impact on the strain distribution ahead of a propagating crack relative to that of a stationary crack.*

*The tensile stress ahead of the crack tip is nearly identical for stationary and propagating cracks in perfectly plastic materials; however differences do increase with the degree of strain hardening.^[22] Nonetheless, this difference remains relatively small compared with the difference found between the strain fields of stationary and propagating cracks.

Although the unique strain field for propagating cracks has been recognized as an important variable affecting subcritical cracking in various environments including gaseous hydrogen, such fields have not been contrasted with those for stationary cracks to interpret differences in subcritical cracking thresholds. For example, the propagating crack strain field has been used to determine the crack-tip strain-rate which controls the passive film rupture frequency during stress corrosion cracking in aqueous solutions, *e.g.*^[23,24] Additionally, the propagating crack strain distribution has been used to inform estimates of critical distances needed for fracture threshold models.^[25,26] The emphasis of the present work is to demonstrate that differences in the strain-controlled, subcritical cracking thresholds measured at crack arrest and at crack initiation can be interpreted based on the respective crack-tip strain fields.

II. EXPERIMENTAL PROCEDURES

A. Materials

Eleven heats of commercially produced Cr-Mo and Ni-Cr-Mo low-alloy pressure vessel steels were examined in this study. Five different heats of SA372 grade *J* and two different heats each of DOT-3T, DOT-3AAX (4130X), and SA372 grade *L* with variations in chemistry and/or strength were tested. The steel designations SA372 grade *J*, DOT-3T, and 4130X refer to Cr-Mo varieties comparable to AISI 41xx, and the SA372 grade *L* is a Ni-Cr-Mo steel comparable to AISI 4340. The yield and tensile strengths as well as alloy compositions shown in Tables I and II were reported by the manufacturer. These pressure vessel steels were acquired as curved panels cut from seamless pipe test-rings, which were heat treated concurrently with commercial pressure vessels and thus have representative microstructures. The heat treatment of the steel test-rings followed a commercial sequence consisting of austenitizing, one-sided quenching, and tempering to achieve the desired strength with proprietary temperatures and durations. The tempered microstructures contain varying amounts of ferrite, bainite and tempered martensite. Representative microstructures of the various pressure vessel steels are shown in Figure 1.

Two fracture toughness specimens machined from the DOT-3T (heat *B* in Table I) were tested in laboratory air following procedures similar to those described in Section II-C. The fracture toughness of this steel, J_{Ic} ,

was $\sim 120 \text{ kJ/m}^2$ ($K_{J_{Ic}} = 165 \text{ MPa } \sqrt{\text{m}}$). The other steels in this study are expected to have comparable or greater values of fracture toughness.

B. Constant-Displacement Threshold Tests

Wedge-opening-load (WOL) specimens for fixed-displacement, subcritical cracking experiments were fabricated following ASTM E1681-03 with the width dimension (W) equal to 56.9 mm, as shown in Figure 2. The WOL specimens were oriented so that the loading and crack-growth directions were parallel to the circumferential and longitudinal axes, respectively, of the original seamless tube (*C-L* orientation). The SA372 grade *J* and grade *L* tubular products had a nominal outer diameter of 510 mm and nominal wall thickness of 38 mm which was sufficient to remove 22.2 mm thick specimens from the mid-radius position of the wall. The 4130X and DOT-3T tubular products had nominal wall thicknesses of ~ 17 and 14 mm, respectively. For these steels, the full wall thickness was utilized for the specimen such that the specimen side faces were curved. The degree of curvature in the specimen varies with the respective diameter of the tubular product, *e.g.*, the outer diameter was ~ 560 mm for the DOT-3T and 630 mm for the 4130X. Side-grooves were machined along the faces of the WOL specimens prior to pre-cracking, which reduced the specimen thickness by 16 pct at the crack plane. Specimens were cleaned using a sequence of degreaser and isopropyl alcohol to remove machining oils and were subsequently handled to prevent contamination (*e.g.*, personnel used rubber gloves).

Pre-cracking was accomplished *via* cyclic loading in air using a servo-hydraulic load frame at 10 Hz using an *R*-ratio (K_{\min}/K_{\max}) equal to 0.1, resulting in ~ 3 mm of fatigue crack growth from the starter notch. The final total crack length and maximum stress-intensity factor (K_{\max}) were 0.55 W and 27 $\text{MPa } \sqrt{\text{m}}$, respectively. Upon completion of pre-cracking, the final compliance of each specimen was recorded. The specimens were then placed into a glovebox filled with ~ 0.1 MPa purified argon containing oxygen and moisture levels controlled to below 2 vppm O_2 and 8 vppm H_2O to minimize further formation of surface oxide at the pre-crack tip.

The crack opening displacement was applied to the pre-cracked WOL specimens inside the glovebox using either A-286 stainless steel bolts or Cu-Be bolts reacting against Cu-Be load tups. The load tups were instrumented with strain gages and act as load sensors. Crack opening displacement was monitored during loading of the bolts using a clip gauge on the front face. This displacement measurement and the measured compliance of the specimen was used to infer the actual load applied to the specimen since this method proved more consistently accurate than estimating load from the output of the load tup.^[20] The load tups did, however, provide a very sensitive means for detecting the onset and arrest of subcritical cracking and were used for calculations of crack growth velocity, which are available in Reference 20. Several additional specimens were prepared using the procedures described above except

Table I. Yield Strength and Composition of the Pressure Vessel Steels

Alloy	Yield Strength (MPa)	C	Cr	Cu	Mo	Ni	Al	Mn	Si	P	S	Fe
4130X	607	0.29	0.92	nr	0.19	nr	0.035	0.62	0.28	0.008	0.004	bal
4130X	641	0.30	0.95	nr	0.18	nr	0.030	0.63	0.28	0.008	0.005	bal
SA372 grade J	641	0.46	0.94	nr	0.18	nr	nr	0.92	0.25	0.011	0.006	bal
SA372 grade J	717	0.48	0.96	nr	0.18	nr	0.026	0.92	0.30	0.010	0.002	bal
SA372 grade J	730	0.48	1.01	nr	0.19	nr	nr	0.98	0.27	0.013	0.005	bal
SA372 grade J	736	0.47	0.96	nr	0.19	nr	0.032	0.92	0.30	0.012	0.003	bal
SA372 grade J	783	0.49	0.99	nr	0.18	nr	nr	0.93	0.28	0.008	0.004	bal
SA372 grade L	731	0.4	0.82	0.1	0.26	1.93	0.022	0.75	0.28	0.006	0.007	bal
SA372 grade L	1053	0.4	0.82	0.1	0.26	1.93	0.022	0.75	0.28	0.006	0.007	bal
DOT-3T	900 A	0.45	0.97	nr	0.18	nr	0.034	0.86	0.25	0.013	0.006	bal
DOT-3T	900 B	0.44	0.99	nr	0.18	nr	0.031	0.85	0.26	0.007	0.003	bal

nr = not reported.

that the crack opening displacement was applied with the specimen exposed to laboratory air rather than the glovebox environment.

These constant-displacement fracture mechanics test methods differ from rising-displacement test methods in two notable ways: (1) loading and hydrogen exposure are sequential for the constant-displacement tests; in contrast, these processes are concurrent for the rising-displacement tests, and (2) constant-displacement tests measure the subcritical cracking threshold from the arrest of a propagating crack, while rising-displacement tests measure the threshold at the onset of subcritical cracking from a stationary crack. When the WOL specimen is loaded to a fixed crack opening displacement and then exposed to hydrogen gas, time-dependent hydrogen uptake reduces the fracture resistance and causes subcritical cracking to extend from the pre-crack. The stress-intensity factor, K , continuously decreases as the crack propagates, until K reaches the threshold stress-intensity factor at crack arrest, K_{THa} .

The crack opening displacement applied to each specimen corresponds to an initial applied stress-intensity factor, K_{app} . While K_{app} must be greater than K_{THa} in order for the crack to extend during testing in hydrogen gas, it must also be low enough so that the crack does not extend through the entire width of the specimen. Once an initial value of K_{THa} was measured for a steel, K_{app} and the associated displacements on subsequent specimens were selected in an attempt to have a range of final crack lengths at crack arrest. Both K_{app} and K_{THa} were calculated based on the applied front face crack opening displacement (V_{FF}), the elastic modulus (E), the specimen width (W), and the crack length-to-width ratio (a/W), using the relationship provided in ASTM E1681:

$$K = \left[V_{FF} E / W^{1/2} \right] [1 - a/W]^{1/2} f(a/W)$$

$$f(a/W) = 0.654 - 1.88(a/W) + 2.66(a/W)^2 - 1.233(a/W)^3$$

[1]

Side-grooves are not explicitly accounted for in E1681 so a small correction factor was applied to account for

their effect on the K solution, as described in Reference 19. The slight side-face curvature in specimens from DOT-3T and 4130X steels was determined to have an insignificant effect on these K calculations.^[20]

The bolt-loaded specimens were placed into a stainless steel pressure vessel, which was sealed while still inside the glovebox. The sealed pressure vessel was then removed from the glovebox, placed inside of a secondary containment vessel, and connected to the gas distribution manifold. All manifold tubing leading up to the pressure vessel valve was purged using three consecutive sequences of vacuum followed by backfilling with 21 MPa helium gas and then an additional three consecutive sequences of vacuum followed by backfilling with 21 MPa hydrogen gas. Immediately following these purging cycles on the manifold, the pressure vessel valve was opened and the residual argon was removed using vacuum. 99.9999 pct pure hydrogen gas was used for manifold purging as well as for the final fill to the test pressure of 103 MPa. Signals from the load tups were recorded continuously *via* electrical feed-throughs in the pressure vessel. The pressure vessels and load tups are the same hardware as reported in Reference 27.

After the pressure vessels were filled with hydrogen gas to the test pressure, subcritical cracking was detected as a drop in the measured load from the instrumented load tups. The incubation time, *i.e.*, the duration of hydrogen gas exposure prior to the onset of subcritical crack growth, varied greatly among specimens, as discussed in Sections III and IV. As such, some pressure vessels were vented and specimens removed after extended times ranging from 170 h to more than 3800 h. Some specimens did not exhibit subcritical cracking in hydrogen gas; many of these were removed from the pressure vessel while inside the glovebox, re-loaded to higher K_{app} values, and then re-tested in hydrogen gas.

At the completion of each test, hydrogen was vented from the pressure vessel. Gas samples were collected at the end of selected tests and sent to a commercial laboratory for compositional analysis. In total, hydrogen gas was sampled from 7 pressure vessels, each of which contained up to eight WOL specimens. The

Table II. Results from Constant-Displacement and Rising-Displacement Threshold Tests

Alloy	Tensile Properties		Constant Displacement			Rising Displacement			
	Yield Strength (MPa)	Tensile Strength (MPa)	# WOL Specimens	K_{THa} (MPa \sqrt{m})	# C(T) Specimens	J_i (kJ/m ²)	J_{THi} (kJ/m ²)	dJ_H/da (kJ/m ² /mm)	K_{THi} (MPa \sqrt{m})
4130X	607	765	1	98	2	7.4	12.2	22.7	53
SA372 grade J	641	786	4	98	—	—	—	—	—
	641	839	—	nep	2	7.8	13.2	25.7	55
	717	852	5	101	—	—	—	—	—
	730	870	2	110	2	9	12	16.3	53
	736	861	5	101	2	10.8	15.7	23.7	60
DOT-3T	783	907	4	81	1	6.1	9.6	16.9	47
	900 A	1001	4	37	2	2.4	3.1	3.3	26
	900 B	1001	3	31	—	—	—	—	—
SA372 grade L	731	873	4	84	—	—	—	—	—
	1053	1149	3	24	1	0.26	0.86	2.8	14
Average values for each heat are shown.									

results from these seven samples demonstrated that water vapor was typically 0.5 to 0.8 vppm, oxygen was less than 0.5 vppm, and CO₂ was less than 0.6 vppm. Hydrocarbons, CO, and NO were less than the detection limit of 0.1 vppm. Up to 5 vppm nitrogen and 18 vppm argon were detected; these argon levels were expected since the test vessels were initially filled with argon while in the glovebox. Due to the consistency of these results and the purging procedures used, the gas was not sampled from all tests.

Additional WOL specimens were machined from 4130X (607 MPa), DOT-3T (900 MPa *B*) and one heat of SA372 grade *J* (736 MPa) which were modified to replace the standard straight-through crack starter notch with a chevron notch. The chevron-notched specimens enabled the use of short pre-crack lengths (*e.g.*, 0.3 W), which led to shorter arrested crack lengths. (Such short pre-crack lengths were not practical with the straight-notch specimens, since these short initial crack lengths required prohibitively high loads at K_{app} ; lower loads can be applied to the chevron-notch specimens since the specimen thickness and associated stiffness are reduced at short crack lengths.) SA372 grade *J* specimens were first machined with a chevron notch having an included angle of about 45 deg. This chevron notch geometry was subsequently modified before machining specimens from the DOT-3T and 4130X such that the chevron included angle was ~30 deg. The chevron notch geometry used for each of these steels is shown in Figure 2.

Specimens that exhibited hydrogen-assisted subcritical cracking were heat tinted for 20 minutes at 553 K (280 °C) to mark the extent of crack propagation and then broken apart. Pre-crack and final crack lengths were measured from digital images using the procedure outlined in ASTM E1820.^[28] Fracture surfaces were examined using standard electron microscopy techniques.

C. Rising-Displacement Threshold Tests

Compact tension (CT) specimens for rising-displacement fracture mechanics experiments were designed according to ASTM Standard E1737-96^[29] with dimensions shown in Figure 2. Conventional rectilinear specimens were extracted from the mid-plane of panels from DOT-3T (900 MPa *A*), 4130X (607 MPa), SA372 grade *J* (641, 730, 736 and 783 MPa) and SA372 grade *L* (1053 MPa). The orientation of the CT specimens relative to the original seamless tubes was the same as the WOL specimens, *i.e.*, *C-L* orientation. Side-grooves were machined along the side faces of the specimens in the same plane as the pre-crack starter notch, which reduced the specimen thickness in this plane by 25 pct. Pre-cracking was performed in laboratory air at 10 Hz and an *R*-ratio of 0.1. A *K*-shedding routine was used in which final K_{max} values equaled 20 MPa \sqrt{m} for all specimens except the DOT-3T and the higher-strength heat of SA372 grade *L* (1053 MPa) in which final K_{max} values equaled 15 MPa \sqrt{m} and 10 MPa \sqrt{m} , respectively. Final pre-crack lengths varied from 0.58 to 0.65 W.

Specimens were tested inside a custom designed stainless steel pressure vessel, which was mounted in the load train of a commercial servo-hydraulic test

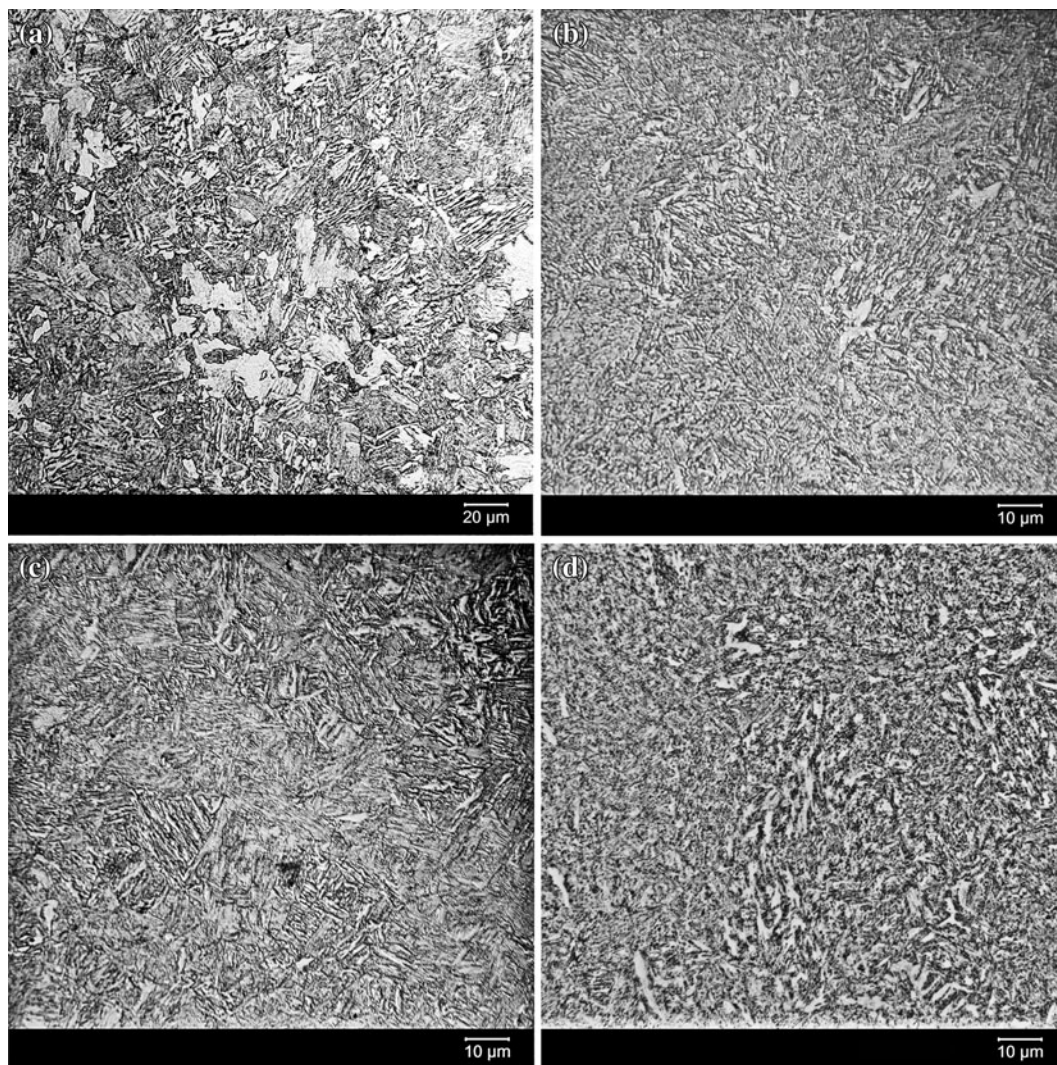


Fig. 1—Optical images showing microstructures of the (a) 4130X, (b) SA372 grade *J* (717 MPa), (c) DOT-3T, (d) SA372 grade *L* (731 MPa). All specimens are etched with Nital and show a surface normal to the radial direction of the original tubular product.

frame. A purging procedure of three pressure-vent cycles using 21 MPa helium followed by three more pressure-vent cycles using 21 MPa hydrogen was used to remove residual gases from the pressure vessel and gas manifold. The vessel was then filled to the test pressure (103 MPa) using 99.9999 pct pure research grade hydrogen. Hydrogen samples taken at the completion of several tests were sent to a commercial testing laboratory for analysis. These results were similar to those reported above for the constant-displacement threshold tests (Section II-B); oxygen was less than 1 vppm but some water vapor levels were moderately higher, *e.g.*, up to 6 vppm.

Load was measured using both the external load cell integrated into the test-frame and a second load cell mounted in series with the specimen inside the pressure vessel. This internal load cell consisted of a linear variable differential transformer (LVDT) in an elastically deforming aluminum ring. While loads measured on the external load cell are affected by friction imparted by the sliding seals in contact with the pull rod, the internal load cell senses only the load sustained by the specimen. Crack-opening displacement was measured

using an LVDT mounted on the front face of the CT specimen. LVDT-based transducers were used to circumvent the effects of pressurized hydrogen on strain gages in conventional transducers. Crack length was continuously monitored using the direct-current potential difference (DCPD) method operating at a current of 3 A. Further details describing the pressure vessel and instrumentation are provided in Reference 20.

Most of the specimens were tested under a constant displacement rate of 0.051 mm/min imposed by the test frame actuator outside the pressure vessel. Over a range of sufficiently high loading rates, it has been demonstrated that increasing the rate leads to higher values of hydrogen-assisted subcritical cracking thresholds^[11,30] since the fracture mechanisms are kinetically limited by hydrogen uptake and transport.^[12] At rates lower than a bounding value, crack extension becomes mechanically, rather than kinetically, limited and subcritical cracking thresholds are not a function of loading rate. Comparison with results from other studies suggests that 0.051 mm/min is slow enough to ensure lower bound threshold measurements^[20,31]; to confirm this expectation,

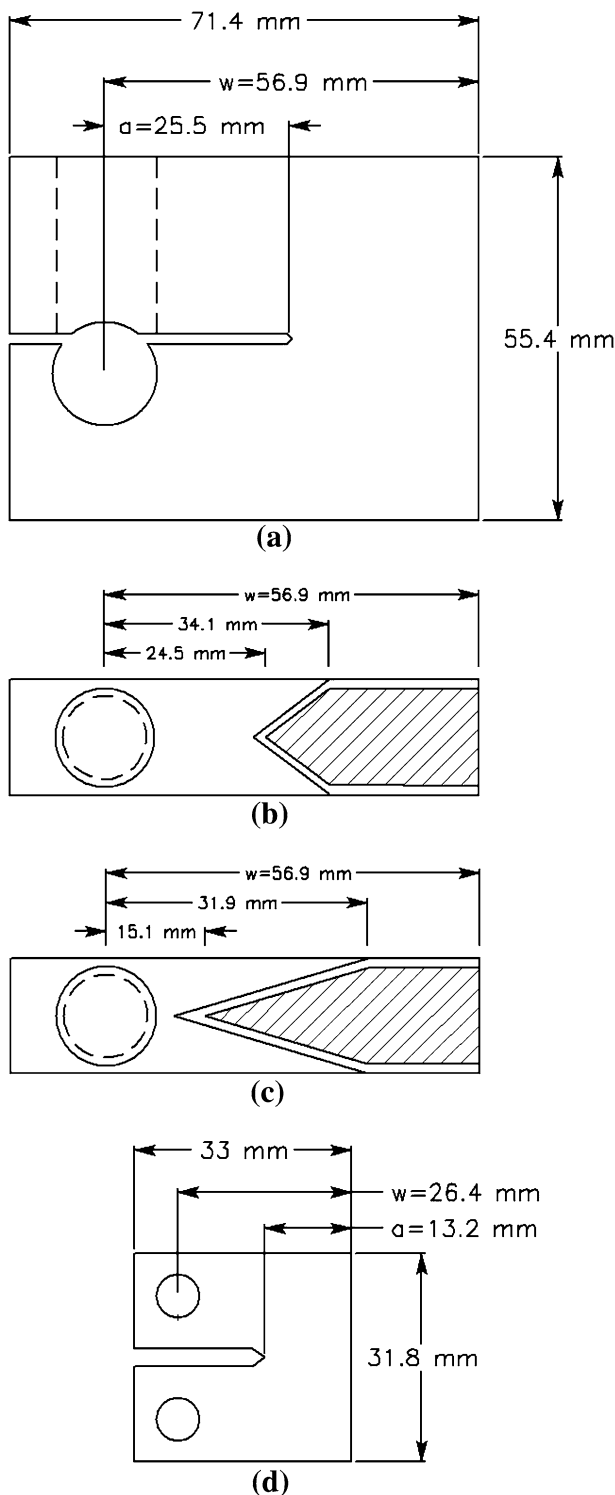


Fig. 2—Specimen drawings showing important dimensions for (a) wedge-opening load (WOL) specimen, (b) SA372 grade J chevron notched WOL specimens, (c) DOT-3T and 4130X chevron notched WOL specimens, and (d) compact tension (CT) specimens.

a replicate specimen of 4130X was tested at 0.0051 mm/min. These displacement rates yield stress-intensity factor rates of ~ 3 MPa $\sqrt{\text{m}}/\text{min}$ and 0.3 MPa $\sqrt{\text{m}}/\text{min}$, respectively, during the initial (elastic) portion of loading.

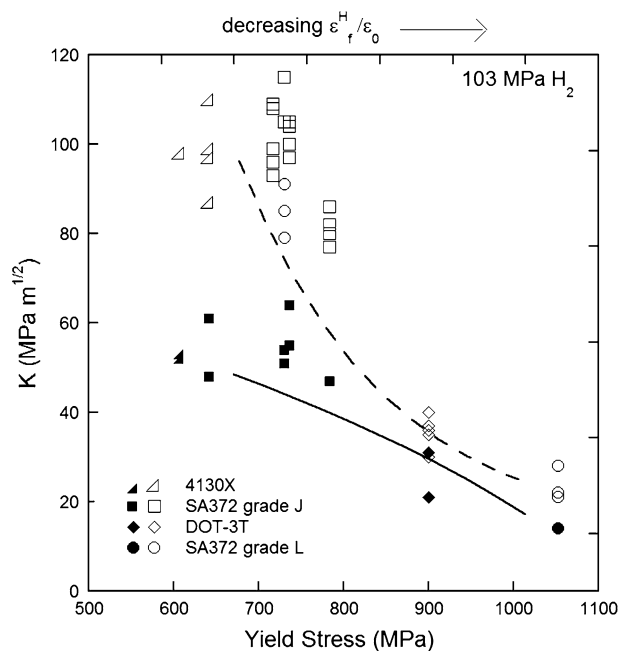


Fig. 3—Crack arrest thresholds in 103 MPa H₂ gas from constant-displacement tests (K_{THa}), open symbols, and crack initiation thresholds from rising-displacement tests (K_{THi}), filled symbols, plotted as a function of yield strength. The solid and dashed lines show general trends of Eqs. [3] and [7], respectively, as a function of ϵ_f^H/ϵ_0 .

The subcritical cracking threshold was invariant at these two loading rates, as presented in Reference 20.

Upon completion of testing, the specimens were heat tinted for 20 minutes at 553 K (280°C). Pre-crack and final crack lengths were measured as described for the WOL specimens in Section II-B. J -integral (J) vs crack extension (Δa) resistance curves (R -curves) were generated using the procedures described in ASTM E1737-96. Crack position was calculated from DCPD measurements using the relationship described by equation A5.1 in ASTM E1737-96. The onset of crack extension was determined from the DCPD data as the first increase in voltage above the initial baseline trend.^[32] DCPD data generally predicted the final crack-length within a few percent of the physically measured value; a linear correction was applied to the crack-length values calculated from the DCPD data to force the final crack-length the match the measured value. Subcritical cracking thresholds are reported (Table II) both as the value of J at the onset of crack extension, J_i , as well as the value of J corresponding to the intersection of the R -curve with the 0.2 mm-offset blunting line (J_{THi}), *i.e.*, following the standardized procedure for defining J_{IC} in inert environments.

III. RESULTS

A. Constant-Displacement Thresholds

Two subcritical cracking thresholds were defined from the constant-displacement tests on WOL specimens in hydrogen gas. The crack-arrest threshold, K_{THa} , was defined in cases when subcritical cracking proceeded from the fatigue pre-crack, and this propagating crack arrested

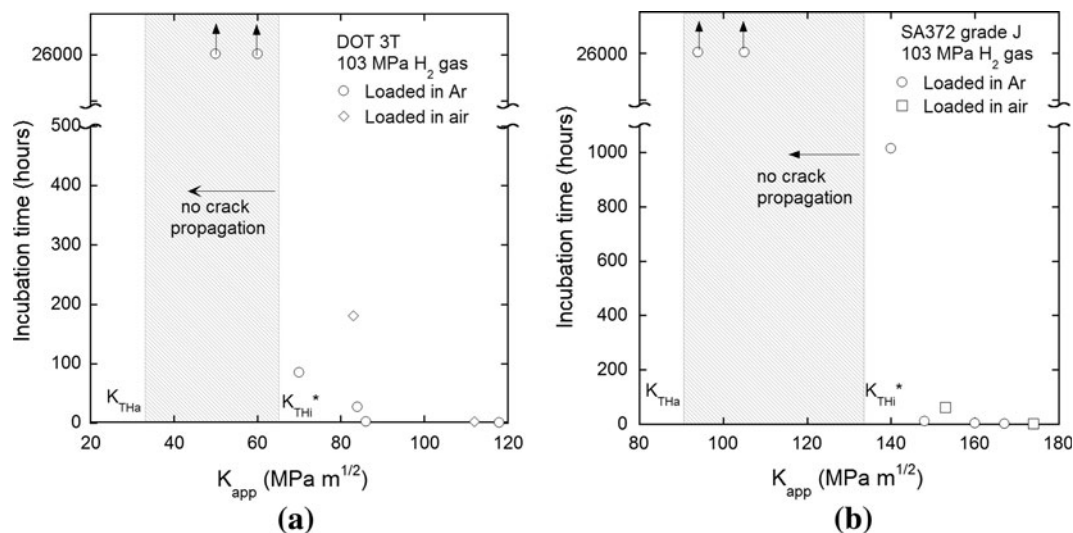


Fig. 4—Plots of incubation time vs K_{app} for (a) DOT-3T and (b) SA372 grade J constant displacement experiments. Data includes specimens that were loaded to K_{app} in argon and in air.

Table III. Largest Values of K_{app} for Which No Crack Propagation (NCP) Was Observed As Well As The Smallest Value of K_{app} for Which Crack Propagation Did Occur for Several of the Alloys Tested

Alloy	K_{THa}	K_{app} NCP	Minimum K_{app} for Crack Propagation	Approx. K_{THi}^*
DOT-3AAX (641 MPa)	87	144	162	$\sim 1.75 K_{THa}$
SA 372 grade J (717 MPa)	93	137	140	$\sim 1.5 K_{THa}$
SA 372 grade J (736 MPa)	97	105	153	$< 1.7 K_{THa}$
SA372 grade L (731 MPa)	79	n/a	134	$< 1.7 K_{THa}$
DOT 3T (900 MPa A)	35	60	83	$< 2.3 K_{THa}$
DOT 3T (900 MPa B)	31	n/a	70	$< 2.3 K_{THa}$
SA372 grade L (1053 MPa)	28	n/a	34	$< 1.2 K_{THa}$

K_{THi}^* is bounded by these two values. The K_{THa} corresponds to the specimen with the smallest value of K_{app} for which crack extension occurred.

as K decreased. In other cases, subcritical cracking did not proceed from the pre-crack, and the K_{app} level was defined as an apparent crack-initiation threshold, K_{THi}^* .

Threshold stress-intensity factors at crack arrest, K_{THa} , were measured for all steels with the exception of one heat of SA372 grade J (641 MPa), for which no subcritical cracking was observed in the two test specimens. The K_{THa} values decrease as a function of increasing yield strength, a typical trend reported in other studies, *e.g.*^[9] Each measured value of K_{THa} measured in 103 MPa hydrogen gas is plotted vs yield strength in Figure 3. Average values of K_{THa} for each steel heat is given in Table II.

Once the stainless steel pressure vessel containing the bolt-loaded specimens was filled with hydrogen, an incubation time preceded the onset of subcritical cracking. Values of incubation time for all specimens are provided in Reference 20. Figure 4 shows representative plots of incubation time vs the initial applied stress-intensity factor, K_{app} , for both heats of DOT-3T and two heats of SA372 grade J (717 and 736 MPa). In all steels, the incubation time generally decreased as K_{app} increased. For steels in which crack propagation did occur, the incubation time could always be reduced to only a few hours or less when K_{app} was about two-fold

greater than K_{THa} . The longest incubation time for any specimen that exhibited crack extension was 1015 h (SA372 grade J (717 MPa) loaded to $K_{app} = 140 \text{ MPa } \sqrt{\text{m}}$). No significant change was observed in K_{THa} or incubation time for specimens that were loaded to K_{app} in air rather than in the glovebox argon environment.

Figure 4 shows that there was a minimum value of K_{app} below which subcritical cracking was never observed. (It must be noted that these K_{app} values exceeded K_{THa} .) This apparent crack initiation threshold value, K_{THi}^* , varies among the steels but was up to two-fold greater than K_{THa} . Values of K_{THi}^* cannot be measured precisely, but may be bounded between the lowest value of K_{app} that caused crack extension to occur in hydrogen and the largest value of K_{app} for which crack propagation did not occur. These bounding values are shown in Table III along with the minimum measured value of K_{THa} for representative heats from each steel specification.

The crack opening displacements required for K_{app} to exceed K_{THi}^* (Figure 4) and ultimately induce subcritical cracking led to crack arrest positions that were generally greater than $a/W = 0.8$. The relative proximity of the

arrested crack tip to the back face of the specimen prompted consideration of a distortion in the crack-tip fields. Consequently, chevron-notched WOL specimens were also tested, since shorter crack lengths at the arrest position (e.g., $a/W = 0.685$) were achieved with these specimens. No correlation was observed between a/W at crack arrest and K_{THa} , leading to the conclusion that crack-arrest thresholds were not affected by the position of the crack tip relative to the back face of the specimen. This conclusion was also supported by finite element modeling which demonstrated K -dominance at the final crack arrest positions, as described in [Appendix](#).

B. Rising-Displacement Thresholds

The subcritical cracking threshold defined from rising-displacement tests on CT specimens in hydrogen gas was the K level at the onset of subcritical cracking from the fatigue pre-crack. This initiation threshold, K_{THi} , was measured for the DOT-3T (900 MPa A), 4130X (607 MPa), SA 372 grade J (641, 730, 736 and 783 MPa), and SA372 Grade L (1053 MPa) steel heats. Since notable plasticity evolved in the CT specimens during loading, particularly for the lower-strength steels, subcritical cracking was characterized using elastic-plastic fracture mechanics methods, i.e., the J -integral. Although hydrogen gas induced subcritical cracking at J levels less than the fracture toughness, J_{IC} , the lower-strength steels still exhibited pronounced crack growth resistance curves (R -curves) as illustrated by the representative J vs Δa plots in Figure 5. The high-resolution DCPD technique was used to identify the onset of subcritical crack extension, and the J -integral value at

this point is defined as J_i . Following conventions in the ASTM standards (E1737, E1820), an additional subcritical cracking threshold, J_{THi} , was defined at the intersection of a 0.2 mm-offset blunting line with the R -curve (Figure 5). All threshold measurements satisfied the criteria of ASTM E1820 for specimen size-independent values of J_{IC} . Both J_i and J_{THi} are tabulated in Table II along with dJ_H/da , the average R -curve slope measured between J_i and J_{THi} . Values of J_i are quite sensitive to the interpretation of the DCPD data whereas J_{THi} is much less sensitive to this subjective variable; as such, J_{THi} is the variable used for most plots and discussion in the following text. To facilitate comparison with the constant-displacement threshold measurements, it is useful to convert J_{THi} to K_{THi} using standard fracture mechanics relationships (see [Appendix](#)). A column of K_{THi} values are listed in Table II.

Data from the constant-displacement and rising-displacement threshold tests (Table II) reveal the notable result that K_{THi} is less than K_{THa} for all steels in this study. This trend is further amplified in Figure 3, in which K_{THa} and K_{THi} are plotted as a function of yield strength. Although K_{THi} and K_{THa} each individually follow the expected trend in which the thresholds decrease as yield strength increases, the difference between K_{THa} and K_{THi} grows as yield strength decreases. Figure 5 and Table II illustrate that dJ_H/da also decreases as the yield strength increases.

C. Fracture Surfaces

All of the steels tested in hydrogen gas using both constant-displacement and rising-displacement methods exhibited similar transgranular fracture surface appearances that were consistent with what has been referred to as plasticity-related hydrogen induced cracking (PRHIC) in martensitic steels.^[33] Unlike other fracture mechanisms such as microvoid coalescence or intergranular fracture, PRHIC fracture surfaces are not characterized by an easily defined, dominant feature. Rather, these transgranular fracture surfaces exhibit fine features that are likely related to the tempered martensite microstructure. Increasing amounts of secondary cracking (perhaps intergranular) were observed on the fracture surfaces of the higher-strength steels such as the DOT-3T and SA372 grade L (1053 MPa). Secondary electron microscopy images of representative fracture surfaces from constant-displacement WOL specimens are shown in Figure 6. Fracture surfaces from the CT specimens tested under rising displacement (Figure 7) are qualitatively similar to those from WOL specimens of the same steel; similarly, fracture surface features on regions of the WOL fracture surfaces corresponding to crack initiation are similar to those regions corresponding to crack arrest. Fracture surfaces from DOT-3T specimens tested under rising displacement in hydrogen gas and in air are shown in Figure 8. Microvoid coalescence (MVC) was the dominant fracture mechanism for the DOT-3T specimens tested in air; fracture of all other steels in air is expected to produce qualitatively similar MVC fracture surface features.

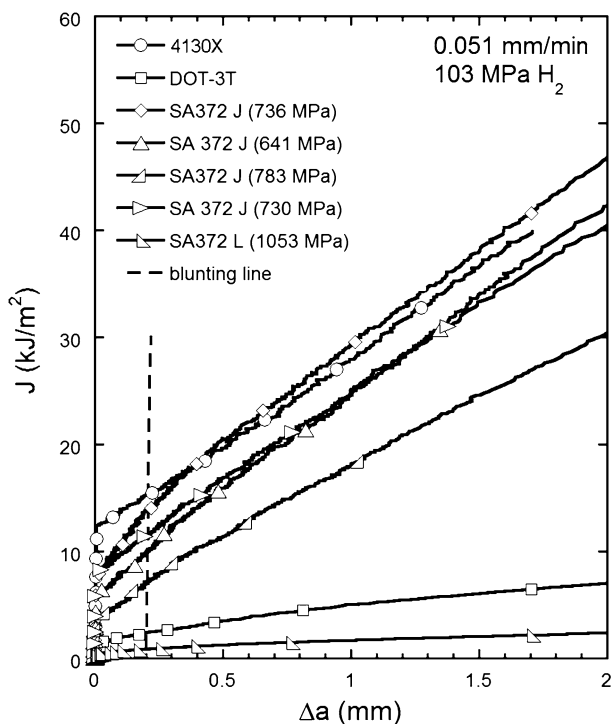


Fig. 5—Crack growth resistance curves (R -curves) for representative specimens from each of the steels tested.

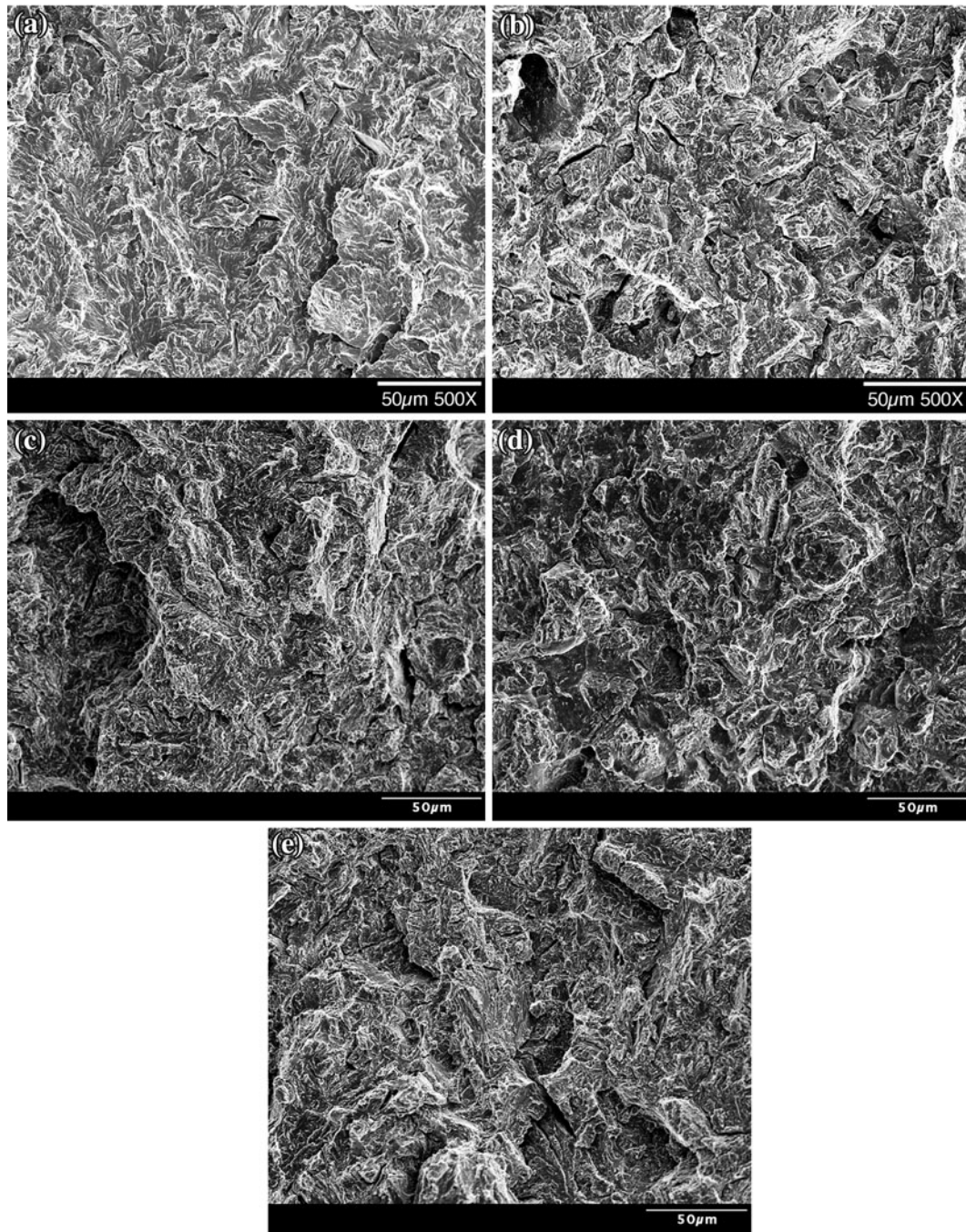


Fig. 6—Secondary electron images of fracture surfaces showing a region near crack arrest from (a) 4130X, (b) DOT-3T, (c) SA372 grade *L* (731 MPa), (d) SA372 grade *L* (1053 MPa), and (e) SA 372 grade *J*.

IV. DISCUSSION

The following discussion first considers the fracture mechanisms for the low-alloy steels tested in hydrogen gas in this study and establishes that hydrogen-assisted fracture is governed by strain-based micromechanics. The implications of a critical strain-based fracture criterion are considered for the three subcritical cracking thresholds (K_{THi}^* , K_{THa} , and K_{THi}) defined from the two test methods (constant displacement and rising

displacement). It is proposed that concurrent hydrogen exposure and strain accumulation is a necessary condition for lower-bound measurements of the subcritical cracking threshold, *i.e.*, this condition leads to K_{THa} and K_{THi} values that are less than K_{THi}^* . It is also shown that weakening of the crack-tip strain field singularity for a propagating crack relative to that for a stationary crack can account for the observation that crack-arrest thresholds, K_{THa} , are higher than crack-initiation thresholds, K_{THi} .

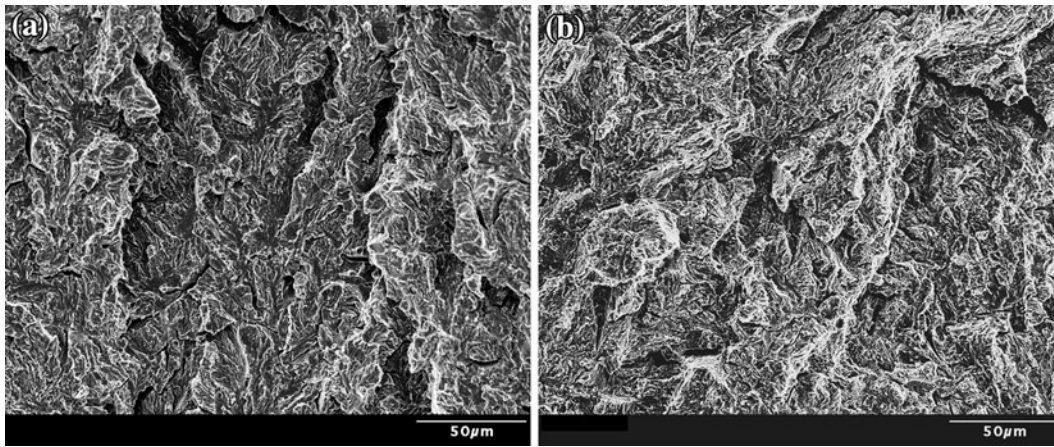


Fig. 7—Secondary electron images of fracture surfaces near initiation from rising-displacement threshold specimens (a) 4130X and (b) SA372 grade J.

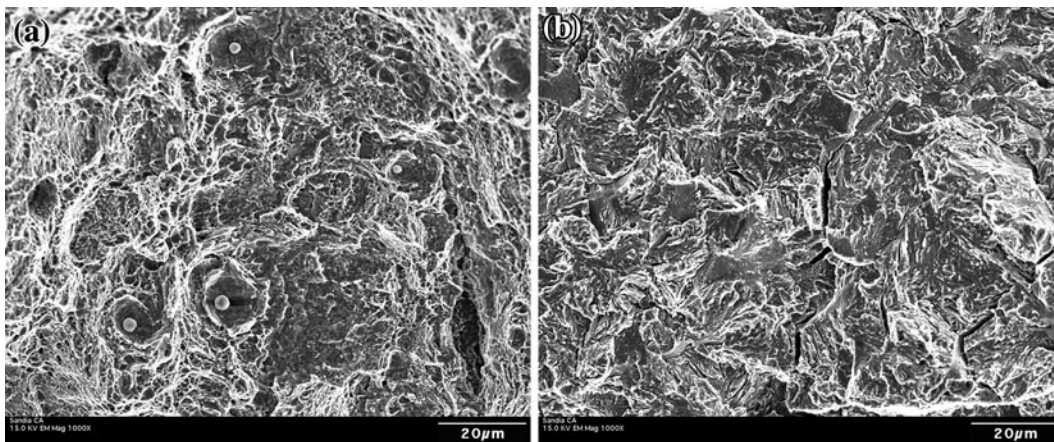


Fig. 8—Fracture surfaces from DOT-3T CT specimens tested under rising displacement in (a) laboratory air and (b) 103 MPa gaseous hydrogen.

A. Mechanisms of Hydrogen-Assisted Fracture

A common fracture mechanism is presumed to operate in the low-to-intermediate strength, tempered low-alloy steels tested in hydrogen gas under both constant and rising displacement in this study, since the fracture surface appearances are similar for all steels and testing conditions (Figures 6 and 7). It is difficult to define precise fracture mechanism details due to the complex fracture surface features, but these features are similar to those observed for hydrogen-assisted fracture in quenched and tempered steels with similar strength levels. Based on fracture surface appearance, the fracture mechanism is often referred to as “quasi-cleavage”^[34–36]; however, as discussed in Reference 20 tracing this term in the technical literature reveals that “quasi-cleavage” is no longer associated with a unique mechanism since fracture surface appearances presumably resulting from a variety of fracture mechanisms have been described as “quasi-cleavage”.^[37–45] Since the term “quasi-cleavage” has been associated with a variety of fracture surface appearances and their characteristic fracture mechanisms, applying the term to hydrogen-assisted fracture in low-to-intermediate strength

low-alloy steels only obscures the details of the true fracture mechanism. There is, however, general agreement that the fracture surface appearance in Figures 6 and 7 results from fracture mechanisms involving plasticity^[20,33,46–48]; recent TEM studies of focused-ion-beam extracted thin films from underneath the fracture surface in mild steels clearly show extensive plasticity-mediated deformation in the presence of hydrogen.^[42,49]

Recognizing the consequence of invoking terminology that does not consider the fracture mechanism, Takeda and McMahon refer to the fracture mechanism in a low-alloy tempered steel tested in hydrogen gas as plasticity-related hydrogen induced cracking (PRHIC),^[33] in order to focus on the role of plasticity in the fracture process. Speculatively, PRHIC involves some combination of initial stress-controlled microcrack formation, followed by strain-controlled linking of these microcracks. Possibilities for the origin of the initial hydrogen-assisted damage nucleation in low-alloy steels include shear band intersections,^[42] martensite lath boundaries^[33] or decohesion along glide planes.^[33] The general concept of PRHIC is consistent with the original intent of the term

quasi-cleavage,^[39] *i.e.*, sequential stress- and strain-controlled fracture processes. In this sense, PRHIC is similar to MVC, the conventional ductile fracture process, in that macroscopic crack propagation results from stress-controlled initial damage, *i.e.*, voids, that subsequently grow and coalesce as a result of accumulated plastic deformation.

Another presumed parallel between MVC and PRHIC is that stress-controlled damage nucleation is driven by both the remote stress as well as local, microstructure-scale stresses. For MVC, it is well established that strain incompatibilities between the matrix and rigid inclusion particles lead to the development of dislocation structures at the particles, producing high local stresses that facilitate void nucleation.^[50] Although the precise damage nucleation mechanism in PRHIC has not been identified, it is reasonable to assume that interfaces in martensitic steels are resistant to slip transmission, and thus strain incompatibilities and associated local stress concentrations contribute to stress-controlled damage nucleation. Following damage nucleation, local plastic strain drives growth and eventual coalescence of this initial damage into a macroscopic crack. Plastic strain is therefore featured in both stages of the fracture process: it leads to microstructure-scale stresses that facilitate damage nucleation, and it drives subsequent damage evolution. The overall fracture process can be characterized as strain controlled.

The distribution and magnitude of microstructure-scale stresses that facilitate damage nucleation in the low-alloy steels may vary for crack propagation in air *vis-à-vis* hydrogen, since the microstructure sites involved in damage nucleation are indisputably different for the two environments (Figure 8). For example, crack propagation in air involves void nucleation at inclusions (*e.g.*, oxides, sulfides). The conspicuous absence of these damage-nucleating particles from the fracture surfaces produced in hydrogen suggests that more intense microstructure-scale stresses may evolve at other sites. One possible reason for variation in microstructure-scale stresses is the relative severity of localized deformation.

It is firmly established that hydrogen facilitates dislocation motion *via* the hydrogen-enhanced localized plasticity (HELP) mechanism in a wide range of metals, including engineering alloys,^[51,52] which can lead to more severe localized deformation.^[53] This localized deformation magnifies strain incompatibilities, resulting in more intense microstructure-scale stresses. Based on this scenario, hydrogen alters the relationship between the continuum strain (which reflects the remote loading conditions) and the local strain (which develops at the microstructural scale), *e.g.*, for a given increment of continuum strain, local strains are higher in hydrogen-exposed materials due to strain localization.^[54,55] Accordingly, lower values of continuum strain are required to attain a threshold level of microstructure-scale stresses for driving damage nucleation.

The notion that PRHIC in low-alloy steels is strain-controlled, and in particular is governed by plastic strain, is supported by the observation of distinct

R-curve behavior during the rising-displacement tests in hydrogen gas (Figure 5). *R*-curve behavior in engineering alloys results from weakening of the crack-tip strain singularity as a stationary crack transitions into a propagating crack,^[21] as discussed in Section IV-C. Since the transition from a stationary crack to a propagating crack does not significantly affect the peak stress ahead of the crack-tip, the increasing remote loading (*K* or *J*) reflected in the *R* curve indicates that the fracture micromechanics is governed by the strain field. Indeed, all models of *R*-curve behavior are based on a strain-controlled fracture criterion, *e.g.*,^[56–58] Thus, the following sections presume that PRHIC is ultimately driven by plastic strain, consistent with the original perspective of Takeda and McMahon.^[33]

The attainment of a critical continuum crack-tip strain, ε_f , can be invoked as the fracture criterion for mechanisms which are governed by plastic strain (see Section IV-C for a more complete description of this criterion). The continuum strain, ε , is dictated by the remote loading condition; the local, microstructure-scale strain is proportional to ε but different in magnitude. Hydrogen alters the relationship between ε and the local strain as a result of the HELP mechanism such that lower values of ε are necessary to attain the same magnitude of local strain. It is important to emphasize that hydrogen exposure and strain accumulation must be concurrent in order to affect this relationship between continuum and local strains. Continuum crack-tip strain which evolves in concert with hydrogen exposure is denoted as ε^H in the discussion that follows. Since hydrogen leads to subcritical cracking thresholds that are less than the fracture toughness, and since fracture requires attainment of a critical value of ε , it follows that the fracture strain in hydrogen, ε_f^H , is less than the fracture strain in inert environments, ε_f . This reduction in hydrogen-affected fracture strain results in part from the altered relationship between continuum strain and local strain, *i.e.*, for a given increment of continuum strain, local strains are higher in the presence of hydrogen.

B. Relationship Between Crack-Tip Strain and Threshold K_{THi}^*

The apparent initiation threshold, K_{THi}^* , is a practical minimum K_{app} value below which subcritical cracking does not proceed from the fatigue pre-crack regardless of how long the constant-displacement WOL specimen is exposed to hydrogen. In the current study, some specimens loaded to stress-intensity factors between K_{THa} and K_{THi}^* were exposed to hydrogen gas for over 26,000 h with no indication of subcritical crack extension. K_{THi}^* is identified in Figure 4 and is represented approximately by the right edge of the shaded areas. The left edge of the shaded areas in Figure 4 represents an average value of the crack-arrest threshold, K_{THa} , which is clearly much less than K_{THi}^* .

In this section, it is proposed that concurrent hydrogen exposure and strain accumulation is necessary to induce the PRHIC fracture mechanism and therefore

that strain-controlled hydrogen-assisted fracture is dependant on both the mechanical and environmental exposure histories. The mechanical and environmental exposure histories vary for K_{THa} and K_{THi}^* and this leads to the difference in their measured values. In the case of K_{THi}^* , remote loading (*i.e.*, imposing K_{app}) and evolution of the associated crack-tip strain precede hydrogen exposure. In contrast, K_{THa} represents a threshold measured under concurrent straining and hydrogen exposure, since the propagating subcritical crack generates its own strain increments (see Section IV-C) while the crack tip is exposed to the hydrogen environment. Considering the discussion in Section IV-A, concurrent strain accumulation and hydrogen exposure may be a necessary condition for the PRHC fracture mechanism. The strain accumulated during loading to K_{app} cannot directly contribute to ε^H since it evolves prior to hydrogen exposure. Instead, since hydrogen exposure follows loading to K_{app} , any concurrent strain accumulation and hydrogen exposure must occur under static-loading conditions. For subcritical cracking to proceed under static loading, a sufficient quantity of crack-tip creep strain must contribute to the hydrogen-deformation interaction represented by ε^H , leading to crack initiation. The strain accumulated during loading to K_{app} creates deformation structures ahead of the crack-tip that may affect the fracture criterion for subsequent crack extension. However, fracture surfaces at crack initiation and crack arrest in the constant displacement specimens as well as in the rising displacement specimen all exhibit very similar features suggesting that the fracture mechanism is not significantly affected by variations in deformation structures formed prior to crack extension. Furthermore, experiments which have applied various levels of plastic strain to test specimens prior to pre-charging with hydrogen have found that this pre-strain has a modest effect on subsequent hydrogen-assisted cracking behavior.^[36,59]

In support of this scenario that crack tip creep is responsible for the attainment of ε^H , it is noted that creep occurs at room temperature as a result of thermally activated dislocation glide.^[60–63] Furthermore, hydrogen has been shown to amplify this low-temperature creep process.^[5,51,64–67] Low-temperature crack-tip creep under static-loading conditions is recognized as essential for mechanically rupturing crack surface oxides during stress corrosion cracking,^[23,68–70] however the contribution of crack-tip creep to strain-controlled hydrogen-assisted fracture has not previously been considered. After constant-displacement WOL specimens are loaded to K_{app} in an inert environment and subsequently exposed to hydrogen gas, accumulated creep strain interacts with hydrogen, leading to localized deformation, microstructure-scale stress concentrations, and damage initiation at microstructure sites characteristic of PRHC.

The strain that accumulates during hydrogen exposure, ε^H , representing hydrogen-deformation interactions during crack-tip creep, only leads to subcritical crack initiation at $K_{app} > K_{THi}^*$ if it exceeds a critical value, ε_F^H . The relationship between a strain-based crack-tip fracture criterion and the remote loading (K)

is described in greater detail in Section IV-C (*e.g.*, see Eq. [3]). In this case, increasing the value of K_{app} increases the magnitude of the crack-tip stress field, and it is this stress field that drives the crack-tip creep. If the crack-tip stress associated with K_{app} is not sufficient for the accumulated crack-tip strain, ε^H , to exceed ε_F^H , then the crack does not extend at that value of K_{app} .

This crack-tip micromechanics interpretation of K_{THi}^* underscores that strain-controlled, hydrogen-assisted fracture is dependant on both the mechanical and environmental exposure histories. Figure 9 illustrates three possible scenarios for loading history relative to hydrogen exposure history pertinent to the threshold tests in this study and indicates why K_{THi}^* is not viewed as a true threshold for the onset of hydrogen-assisted subcritical cracking, in contrast to K_{THi} . When loading is concurrent with hydrogen exposure (rising-displacement K_{THi} measurements, Figure 9(a)), hydrogen interacts with the crack-tip deformation throughout the loading history. Consequently, the strain accumulated during hydrogen exposure, ε^H , increases as K increases and subcritical cracking proceeds when $\varepsilon^H = \varepsilon_F^H$. (Recall from Section IV-A that ε^H is a continuum strain quantity representing hydrogen-affected deformation, *i.e.*, presuming ε and ε^H represent the same continuum strain level, the latter quantity reflects more severely localized strain.) Figures 9(b) and (c) depict how the scenario changes when loading precedes hydrogen exposure (constant-displacement K_{THi}^* and K_{THa} measurements). In this case, strain that accumulates during loading does not contribute to ε^H . Only the creep strain which accumulates during hydrogen exposure under static loading contributes to ε^H . Therefore, the magnitude of K_{app} dictates whether subcritical cracking proceeds, since the associated crack-tip stress governs the accumulated crack-tip creep strain under hydrogen exposure, leading to crack extension at ε_F^H .**

**Quantitative analyses should consider that the value of ε_F^H may not be identical for constant displacement and rising displacement test conditions.

The scenario in Figure 9(b) portrays the conditions associated with tests having $K_{app} < K_{THi}^*$. In Figure 9(b), $K_{app} = K_3$ represents the static-loading condition on the specimen prior to hydrogen exposure. (As suggested by Figure 9(a), K_3 is sufficient to initiate subcritical cracking if loading and hydrogen exposure are concurrent.) K_{app} is then maintained at K_3 as the specimen is exposed to hydrogen gas, and creep strain accumulates and interacts with hydrogen at the crack tip. The creep strain rate decays with time since the remote applied crack opening displacement (and K_{app}) remains static.^[68,69] In this case, K_3 is insufficient in magnitude to drive ε^H to the level of ε_F^H so subcritical cracking never initiates, *i.e.*, K_3 is less than K_{THi}^* in Figure 9(b).

The scenario in Figure 9(c) represents conditions associated with tests having $K_{app} > K_{THi}^*$. When higher K_{app} is applied to the specimen, greater creep strain rates evolve in response to the higher crack-tip stress^[69] and

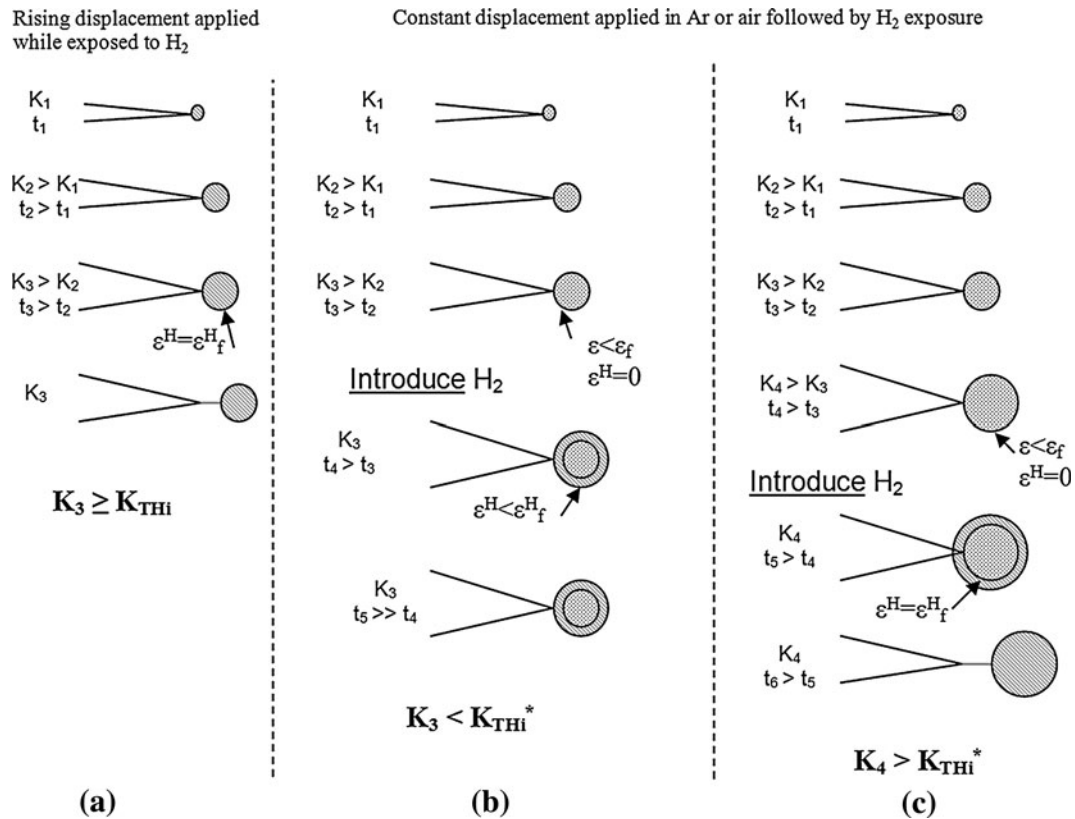


Fig. 9—The process by which increasing K_{app} leads to the development of the crack-tip plastic zone. Ultimately crack propagation differs when loading is concurrent with hydrogen exposure (a) relative to when loading in an inert environment precedes hydrogen exposure (b) and (c).

thus the accumulated strain in hydrogen, ϵ^H , is enhanced. If this strain exceeds ϵ_f^H , then subcritical cracking initiates. In the example shown in Figure 9(c), sufficient strain has accumulated under hydrogen exposure for subcritical cracking to initiate at K_4 , which is higher than K_{THi}^* . At this condition, ϵ^H exceeds ϵ_f^H but still contributes only a portion of the total crack tip strain, since much of the total crack tip strain accumulated prior to hydrogen exposure.

Following subcritical crack initiation in hydrogen gas, the strain field progresses with the crack tip such that strain accumulated at successive crack positions represents hydrogen-affected deformation and contributes to ϵ^H . As the crack tip moves from its initial position, the total crack tip strain decreases, however ϵ^H contributes an increasing portion such that ϵ^H exceeds ϵ_f^H at all subsequent crack positions. Since the total strain decreases with crack extension, the condition for crack arrest is again $\epsilon^H = \epsilon_f^H$. Therefore, K_{THa} is a crack-arrest threshold which is not a function of hydrogen exposure history, however its characteristics as a subcritical cracking threshold are still strongly influenced by deformation history, as discussed in Section IV-C.

In support of the preceding interpretation of the relationship between crack-tip strain and K_{THi}^* , it is noted that other suggestions for the absence of subcritical cracking under constant displacement can be eliminated for the experiments in this study. In previous reports,^[33,71] it was suggested that the absence of subcritical crack propagation for $K_{app} > K_{THa}$ could

be attributed to hydrogen-induced bifurcation of the primary crack tip during initial crack extension, since crack bifurcation could lead to shielding of the K -dominated stress and strain fields and consequently inhibit further crack extension.^[72] While crack bifurcation at the pre-crack tip in specimens with $K_{app} > K_{THi}^*$ was observed, such crack bifurcation was absent in specimens loaded at lower K_{app} , i.e., greater than K_{THa} but less than K_{THi}^* . Since crack bifurcation was not observed for all $K_{app} > K_{THa}$, this phenomenon does not give rise to K_{THi}^* as an apparent threshold for crack initiation.^[20]

Another physical phenomenon that has been invoked to explain non-propagating cracks under high values of K_{app} in low-strength steels is crack-tip blunting.^[9] Given the substantial crack-tip deformation sustained by the lower-strength steels in this study (e.g., 4130X, as described in Appendix), significant crack-tip blunting is expected in these WOL specimens. However, accounting for such deformation through elastic-plastic analysis reveals an increase in the remote crack-driving force, i.e., the J -integral. The details of this analysis are provided in Appendix. In addition, while blunting reduces the crack-tip stress, the high strains associated with blunting enhance the local driving force for strain-controlled fracture.

Standardized test methods, such as ASTM E1681, allow the threshold stress-intensity factor for subcritical cracking to be determined based on the minimum value of K_{app} for which limited or no crack extension occurs

(i.e., K_{THi}^*). The difference between K_{THa} and K_{THi}^* prompts consideration of the meaning of a subcritical cracking threshold. In structural design, the threshold stress-intensity factor is typically assumed to be the K level below which subcritical cracking does not proceed. Although K_{THi}^* appears to satisfy this definition, this parameter is not appropriate in engineering design and structural analysis of hydrogen containment components since it only describes threshold behavior of specimens loaded in an inert environment and then subsequently exposed to hydrogen. These conditions are not representative of a crack-like defect on the internal wall surface of a compressed hydrogen gas component, in which mechanical loading and hydrogen exposure are concurrent.

C. Relationship Between Crack-Tip Strain and Thresholds K_{THa} and K_{THi}

One of the most notable results from this study is that the crack-initiation threshold measured under rising displacement, K_{THi} , is less than the crack-arrest threshold measured under constant displacement, K_{THa} (Figure 3). The difference between K_{THi} and K_{THa} increases as yield strength decreases; however, the overall trend for each data set is that the subcritical cracking threshold in hydrogen gas decreases with increasing yield strength. It is proposed that the disparity between K_{THa} and K_{THi} can be explained by examining differences in the crack-tip strain fields for a stationary crack compared to a propagating crack. This section first presents the strain-based criterion for the onset of crack extension from a stationary crack, as derived from the relevant crack-tip strain field. Next, the crack-tip strain field for a propagating crack is reviewed, and an analogous strain-controlled fracture criterion that models the conditions for arrest of a propagating crack is presented. Finally, the measured K_{THa} and K_{THi} trends are shown to be consistent with the strain-based micromechanical fracture model formulations for stationary and propagating cracks.

1. Strain-controlled fracture criterion for stationary cracks

Strain-controlled crack initiation occurs when the continuum crack-tip strain attains a critical value. Hutchinson^[73] and Rice and Rosengren^[74] demonstrate that the stress and strain distribution ahead of a stationary crack decays as a function of $1/r$ for power law hardening materials, i.e.;

$$\varepsilon_y = k \left(\frac{J}{r} \right)^{\frac{n}{n+1}} \quad [2]$$

where r is the radial distance from the crack tip, n is the strain hardening exponent and k is a scaling parameter. Ritchie *et al.* suggested that crack extension proceeds when the continuum crack-tip strain, ε , exceeds the critical fracture strain, ε_f , over a characteristic distance, l^* , ahead of the crack tip.^[56,75] The characteristic distance is generally associated with the size scale of microstructural damage ahead of the

crack. By virtue of Eq. [2], the relationship between the critical stress-intensity factor, K_{THi} , hydrogen-affected fracture strain, ε_f^H , and characteristic distance, l^* , for a perfectly plastic material, is expressed as^[56]:

$$K_{THi} \approx 6 \sqrt{E \sigma_0 l^* \varepsilon_f^H} = 6 \sigma_0 \sqrt{l^* \frac{\varepsilon_f^H}{\varepsilon_0}} \quad [3]$$

The parameters E and σ_0 are the elastic modulus and yield strength, respectively, and ε_0 refers to the yield strain (e.g., $E = \sigma_0/\varepsilon_0$). Equation [3] indicates that K_{THi} displays a square-root dependence on the critical fracture strain, ε_f^H . Strain-hardening materials exhibit a weaker singularity than that predicted by assumptions of perfectly plastic behavior.^[73,74] For the purpose of this discussion, which is to compare strain-based fracture criteria trends for stationary and propagating cracks, the perfectly plastic assumption inherent to Eq. [3] is satisfactory.

2. Strain-controlled fracture criterion for propagating cracks

Equation [3] describes the micromechanics criterion for strain-controlled crack initiation but does not represent the criterion for continued crack growth because the strain field for a propagating crack differs from that for a stationary crack. While the strain field for a stationary crack decays as $1/r$ and is solely proportional to the remote loading (i.e., K or J), the strain field for a propagating crack decays as $\ln(1/r)$ and is proportional to the remote loading as well as a component associated with the crack extension itself.^[21,76,77] Due to the weaker strain-field singularity for the propagating crack, the magnitude of the strain at a given distance from the tip of a propagating crack is less than that for a stationary crack under the same nominal remote loading (i.e., K or J). Although the micromechanical fracture parameters (e.g., ε_f , l^*) may be invariant for the stationary and propagating cracks, this important difference in the crack-tip strain fields results in higher remote loading to maintain slow, stable crack growth compared to the remote loading to initiate extension of a stationary crack. As a result, materials with strain-controlled fracture criteria can exhibit a crack-growth resistance curve (R -curve), in which increasing remote loading is necessary to sustain crack extension. This increase in remote loading required for each subsequent increment of crack extension gradually decreases until a steady-state condition is reached, at which point crack extension is sustained at a constant value of K or J . These concepts are developed in more detail below.

Establishing relationships between remote loading parameters (K or J) and crack-tip fracture strain requires analytical expressions for the crack-tip strain field. Rice and co-workers developed exact asymptotic solutions for the strain distribution ahead of a propagating crack, which account for elastic unloading in the crack wake and the ensuing non-proportional straining.^[21,78,79] From these results, the equivalent plastic shear strain directly above the tip of a propagating mode

I crack in an elastic-perfectly plastic material under small-scale yielding can be expressed as:

$$\gamma^p = \frac{M dJ}{\sigma_0 da} + \frac{1.88(5-4\nu)\sigma_0}{2E} \ln\left(\frac{r_p}{r}\right) \quad [4]$$

where M is a proportionality constant, σ_0 is the yield strength, dJ/da is the slope of the crack-growth resistance curve (J vs Δa) at the current crack position, ν is Poisson's ratio, r is radial distance from the crack tip, and r_p is a parameter in the asymptotic analysis that can be approximated by the plastic zone radius, *i.e.*, $r_p \propto K^2$ or $r_p \propto J$.^[56] Equation [4] in conjunction with a strain-controlled fracture criterion leads to the following expression for continued crack propagation:

$$\gamma_f^p = \frac{M dJ}{\sigma_0 da} + \frac{1.88(5-4\nu)\sigma_0}{2E} \ln\left(\frac{r_p}{l^*}\right) \quad [5]$$

Here, γ_f^p is the critical value of plastic shear strain required for crack extension. During transient crack growth under increasing remote loading (*i.e.*, prior to reaching steady state), dJ/da decreases and r_p increases such that the first term of Eq. [5] provides a diminishing contribution to further crack extension while the second term provides an enhanced contribution. At steady state (*i.e.*, $dJ/da = 0$), the plastic zone size remains constant at $r_p = r_p^{ss}$ and only the second term in Eq. [5] describes the condition for continued crack propagation, *viz*:

$$\gamma_f^p = \frac{1.88(5-4\nu)\sigma_0}{2E} \ln\left(\frac{r_p^{ss}}{l^*}\right) \quad [6]$$

Equation [6] reflects the fact that crack extension under steady-state conditions is self-sustaining with a plastic zone size ($r_p \propto K^2$) r_p^{ss} .

3. Comparison between micromechanics models and measured thresholds

Although the micromechanics of propagating cracks summarized above was established to understand conventional crack-growth resistance behavior in ductile metals subjected to rising-loading conditions, this concept is adapted to strain-controlled, subcritical crack extension under constant crack-opening displacement, *i.e.*, the WOL experiments on low-alloy steels in hydrogen gas. In particular, it is argued that the functional form of the strain field in Eq. [4] applies to propagating cracks in the constant-displacement WOL experiments. For these experiments in which the remote loading (*i.e.*, K) decreases as subcritical cracking proceeds, the crack-tip micromechanics criterion for crack extension is $\varepsilon^H > \varepsilon_f^H$, where ε^H is related to the remote loading by an expression analogous to Eq. [4]. As K decreases ε^H also decreases, and the criterion for crack arrest is $\varepsilon^H = \varepsilon_f^H$ at $K = K_{THa}$.

Stipulating that the functional form of Eq. [4] pertains to propagating subcritical cracks in the constant-displacement threshold tests, it is further argued that the second term in Eq. [4] provides a bounding condition for the strain field of a crack propagating under decreasing

K , *e.g.*, the strain field of the propagating crack is not less than the quantity described by the second term of Eq. [4]. It is demonstrated below that the presumed dominance of the $\ln(1/r)$ term in Eq. [4] leads to a compelling correlation between crack-tip micromechanics model trends and measured crack-arrest threshold trends. Given this simplification, the criterion for subcritical crack extension and arrest is given by an expression similar to Eq. [6].

The presumed parallels between crack propagation as embodied in the conventional R -curve and crack propagation in the constant-displacement threshold tests allow the development of a micromechanical model for K_{THa} . Employing Eq. [6] as a foundation, Ritchie *et al.* developed an expression between the remote loading during steady-state crack growth (K_{ss}) and the crack-tip fracture strain for an elastic-perfectly plastic material.^[56] Based on the criterion that steady-state crack propagation proceeds when $\varepsilon = \varepsilon_f$, Eq. [6] leads to a relationship between the remote loading (*i.e.*, K_{ss}) and the ratio $\varepsilon_f/\varepsilon_0$. Presuming that an analogous form of Eq. [6] applies at crack arrest in the constant-displacement threshold tests, a similar relationship between K_{THa} and $\varepsilon_f^H/\varepsilon_0$ can be described by the following expression:

$$K_{THa} \approx A\sigma_0\sqrt{l^*} \exp\left(B\frac{\varepsilon_f^H}{\varepsilon_0}\right) \quad [7]$$

where A and B are constants. As expected for strain-controlled fracture, Eq. [7] shows that the crack-arrest threshold depends primarily on the yield stress and strain, σ_0 and ε_0 , fracture strain, ε_f^H , and critical distance, l^* . This expression is also consistent with the expectation that high ratios of fracture strain relative to yield strain (γ_f/γ_0 or $\varepsilon_f/\varepsilon_0$) contribute to increased crack-growth resistance.^[57]

Equation [7], like Eq. [3], is strictly valid only for perfectly plastic materials. Materials exhibiting strain hardening have a weaker strain-field singularity than perfectly plastic materials, however both experimental and analytical studies have shown that the form of the singularity in strain-hardening materials remains consistent with the general form of $(1/r)$ for the stationary crack and $\ln(1/r)$ for the propagating crack, *e.g.*^[80–82] In addition, numerical analysis by Dean and Hutchinson^[57] that accounts for strain hardening shows that whereas Rice's analytical solution (*e.g.* (7)) overestimates the ratio of K_{ss}/K_{Ic} for strain-hardening materials, particularly for materials with very high $\varepsilon_f/\varepsilon_0$, the exponential form of Eq. [7] is not altered. Although strain-hardening leads to an additional uncertainty in the quantitative accuracy of Eqs. [3] and [7] for the steels in the current study, the trends suggested by these equations are not compromised.

Since the critical fracture strain criterion is assumed to be the same for both subcritical cracking thresholds (*i.e.*, initiation and arrest), the salient difference between K_{THi} and K_{THa} is the respective relationship between the remote loading parameter (*e.g.*, K) and the crack-tip strain for stationary and propagating cracks. The presence of the term $\varepsilon_f^H/\varepsilon_0$ within the exponential of Eq. [7] for the arrest threshold, compared to the square-root

dependency in Eq. [3] for the initiation threshold, demonstrates the potential for substantial differences in K_{THa} and K_{THi} when $\varepsilon_f^H \gg \varepsilon_0$. In addition, comparison of Eqs. [3] and [7] suggests that the quantity K_{THa}/K_{THi} converges toward unity as $\varepsilon_f^H/\varepsilon_0$ decreases toward unity. Presuming that $\varepsilon_f^H/\varepsilon_0$ decreases in the low-alloy steels as yield strength increases, it is apparent that the trend expected from Eqs. [3] and [7] is reflected in the data presented in Figure 3 as shown by the solid and dashed curves. These curves represent square root and exponential functions of $\varepsilon_f^H/\varepsilon_0$, respectively; since Eqs. [3] and [7] are not expected to yield quantitatively accurate results for strain hardening materials and since the constant terms are not known, these curves are plotted assuming an arbitrary relationship between $\varepsilon_f^H/\varepsilon_0$ and yield strength. The predicted curves are superimposed on the measured values and are intended only to demonstrate the qualitative trends. These trends correspond convincingly with the measurements of K_{THi} and K_{THa} plotted as a function of yield strength.

The proposed similarity in the crack-tip strain fields for propagating subcritical cracks in constant-displacement threshold tests and propagating cracks in conventional rising-load fracture tests suggests that there is a relationship between K_{THa} and the R -curve measured in hydrogen gas (e.g., Figure 5). Based on stipulations presented earlier in this section, the basic form of the crack-tip strain field in Eq. [4] applies to propagating cracks in the constant-displacement threshold tests. Equation [4] also applies to the propagating cracks in rising-displacement threshold tests that yielded the R -curves in Figure 5. In each case, a form of Eq. [6] leads to micromechanical modeling expressions for either K_{THa} (i.e., Eq. [7]) or K_{SS} . In the latter case, K_{SS} is the resistance to steady-state crack propagation measured under rising displacement in hydrogen gas. This rationale suggests that there is a direct relationship between K_{THa} and K_{SS} measured in hydrogen gas.

Assuming that $K_{THa} \propto K_{SS}$, a model by Rice *et al.*^[78] demonstrates that the measured R -curve provides insight into the magnitude of K_{THa} . In this small-scale yielding model, the ratio of the J -integral during steady-state crack propagation to the fracture initiation toughness (J_{SS}/J_{Ic}) can be determined from only the initial slope of the R -curve ($dJ/da)_0$, viz:

$$\frac{J_{SS}}{J_{Ic}} = \exp\left(\text{const} \frac{E}{\sigma_0^2} \left(\frac{dJ}{da}\right)_0\right) \quad [8]$$

in which the constant is approximately equal to 0.1.^[56] Based on the equivalence of J_{Ic} and K_{THi} as parameters that characterize fracture initiation in inert environments and hydrogen gas, respectively, as well as the proposed relationship between K_{SS} and K_{THa} , the following expression is derived from Eq. [8]:

$$\left(\frac{K_{THa}}{K_{THi}}\right)^2 \propto \left(\frac{K_{SS}}{K_{THi}}\right)^2 = \exp\left(\text{const} \frac{E}{\sigma_0^2} \left(\frac{dJ_H}{da}\right)_0\right) \quad [9]$$

Equation [9] demonstrates that steep R -curves measured in hydrogen gas (i.e., high (dJ_H/da)) are expected

to correlate to measurements of K_{THa} that exceed K_{THi} . When this is the case, K_{THa} is a non-conservative estimate of the subcritical cracking threshold. For example, Figures 3 and 5 show that the 4130X steel exhibits both the highest value of dJ_H/da and the highest ratio of K_{THa}/K_{THi} . In contrast, the nearly flat R -curve for DOT-3T is consistent with K_{THa} values that approach K_{THi} . Despite this potential for equivalent measurements under certain conditions, these two thresholds are not considered to be the same subcritical cracking property.

Attributing the measured threshold trends in Figure 3 exclusively to differences in the crack-tip strain fields as embodied in Eqs. [3] and [7] is solidified by dispatching characteristics of the test methods that could bias the results. Inappropriate selection of displacement rates may affect measurements of K_{THi} (e.g.,^[11]), however, this should only have the effect of inflating values of K_{THi} . Careful consideration of the effect of loading rates suggests that K_{THi} results shown in Figure 3 are expected to represent lower-bound values which are not artificially low.^[20] Additionally, two features of the constant-displacement threshold tests that raised concern were the proximity of the arrested crack tip to the back face of the WOL specimen and the extent of crack-tip deformation at crack arrest, both of which could affect the crack-tip fields and distort the measured value of K_{THa} . However, the analyses provided in Appendix demonstrate that neither of these factors impacted the K_{THa} measurements, and thus the elevated measured values of K_{THa} relative to K_{THi} in Figure 3 were not influenced by extrinsic factors associated with applying the constant-displacement test method to low-to-intermediate strength steels.

Having ruled out other probable causes for measurement inaccuracies, the disparity between K_{THi} and K_{THa} , which is most pronounced at lower yield strength, appears to have an intrinsic source. The mechanistic origin of this intrinsic dissimilarity between rising-displacement and constant-displacement thresholds is explained based on the crack-tip micromechanics framework represented by Eqs. [3] and [7].

D. Technological Implications

Fracture mechanics provides a robust method for damage-tolerant life prediction of structures, however the application of data measured from laboratory specimens to engineered structures requires that similitude is maintained between specimen and structure with regard to both environmental and mechanical crack-tip conditions. Lower-strength, low-alloy steels exhibit relatively high subcritical cracking thresholds as well as strain-controlled fracture modes when tested in 103 MPa hydrogen gas, and thus the plastic strain history at the crack tip must be considered with respect to fracture mechanics similitude. Available data suggest that most hydrogen-related failures of low-alloy steel pressure vessels occur during, or immediately following, filling of the vessel.^[83] Hydrogen gas storage vessels, pipelines, etc. are susceptible to subcritical crack growth during pressurization in which any existing crack is

subjected to an increasing stress-intensity factor while concurrently exposed to hydrogen gas. Use of constant-displacement specimens, in which the load is applied prior to hydrogen exposure, violates assumptions of similitude (e.g., crack-tip strain history relative to hydrogen exposure history) with the intended structural application and is not expected to yield conservative results. This study demonstrates that constant-displacement test methods provide subcritical cracking thresholds that represent fundamentally different properties than the subcritical cracking thresholds measured under rising displacement. These distinct properties are similar only when the fracture mechanism is stress controlled or if the resistance to stable crack growth (i.e., dJ_H/da) is low, conditions most likely encountered only for higher-strength steels. Reliable and conservative subcritical cracking test methods for lower-strength and/or highly cracking resistant materials likely require active-loading measurements of initiation thresholds. Elastic-plastic fracture measurements, such as the J -integral method, enable substantially smaller specimen sizes and therefore are of greater practical use for lower-strength steels.

V. CONCLUSIONS

1. Subcritical cracking thresholds were measured for commercial low-alloy pressure vessel steels (yield strengths between 641 and 1053 MPa) in 103 MPa hydrogen gas using fracture mechanics methods. Three definitions of the subcritical cracking threshold were evaluated, including crack-initiation and crack-arrest thresholds from constant-displacement tests (K_{THi}^* and K_{THa} , respectively) as well as crack-initiation threshold from rising-displacement tests (K_{THi}). Two prominent observations are established: (1) the constant-displacement tests can exhibit an apparent crack-initiation threshold, K_{THi}^* , that exceeds the crack-arrest threshold, K_{THa} ; and (2) the constant-displacement, crack-arrest threshold, K_{THa} , is greater than the rising-displacement, crack-initiation threshold, K_{THi} , and the difference in these threshold measurements increases as the steel yield strength decreases. These data trends are interpreted in a strain-based crack-tip micromechanics framework.
2. Fracture surfaces resulting from hydrogen-assisted subcritical cracking in low-to-intermediate strength martensitic steels is consistent with previous observations of plasticity-related hydrogen induced cracking (PRHC) in martensitic steels. The distinct crack-growth resistance curves measured for these steels in hydrogen gas is consistent with strain controlled fracture mechanisms.
3. Concurrent strain and hydrogen exposure appear to be a necessary condition for the PRHC fracture mechanism.
4. Subcritical cracking thresholds measured at crack arrest, K_{THa} , under constant displacement reflect resistance to crack propagation whereas thresholds, K_{THi} , measured under rising displacement reflect resistance to crack initiation. The difference in

threshold measurements is attributed to the weaker strain field singularity that varies as $\ln(1/r)$ for a propagating crack compared to the singularity that varies as $(1/r)$ for a stationary crack. Under the assumption that the crack-tip fracture strain does not depend on the test method, the weaker strain field singularity of a propagating crack accounts for the observation that K_{THa} is greater than K_{THi} .

5. The magnitude of the difference between K_{THa} and K_{THi} increases as the ratio of the fracture strain to the yield strain, ϵ_f^H/ϵ_0 , increases. Micromechanical models, which predict fracture to occur when a critical plastic strain is accumulated at a critical distance from the crack tip, show that K_{THa} increases proportionally to $\exp(\epsilon_f^H/\epsilon_0)$ whereas K_{THi} increases proportionally to $(\epsilon_f^H/\epsilon_0)^{1/2}$. The quantity ϵ_f^H/ϵ_0 is small for low threshold materials so the values K_{THa} and K_{THi} may be expected to be similar; ϵ_f^H/ϵ_0 is large for high threshold materials so K_{THa} is expected to exceed K_{THi} .
6. Subcritical crack extension proceeds in constant-displacement threshold tests at $K_{app} > K_{THi}^*$ only once the accumulated crack-tip strain in hydrogen, ϵ^H , exceeds the fracture strain, ϵ_f^H . If the fixed displacement is applied in an inert environment prior to hydrogen exposure, additional strain must accumulate in hydrogen to induce hydrogen-assisted subcritical cracking. Crack-tip creep coupled with hydrogen-deformation interactions are responsible for the crack-tip strain accumulation leading to subcritical cracking.
7. Higher applied stress-intensity factors, K_{app} , lead to greater crack-tip creep strains in constant-displacement subcritical cracking threshold tests. Therefore, the apparent threshold stress-intensity factor for crack initiation in a constant-displacement specimen, K_{THi}^* , is a measure of the minimum stress-intensity factor that is required for the accumulated crack-tip strain in hydrogen, ϵ^H , to exceed the critical value, ϵ_f^H .

ACKNOWLEDGMENTS

Sandia National Laboratories is a multi-program laboratory managed and operated by Sandia Corporation, a wholly owned subsidiary of Lockheed Martin Corporation, for the U.S. Department of Energy's National Nuclear Security Administration under contract DE-AC04-94AL85000. The experimental work presented here has been supported by the US Department of Energy Fuel Cell Technologies program through the Safety, Codes and Standards sub-program element. PS and MD were supported by the US Department of Energy under Grant GO15045. The assistance of Ken Lee and Jeff Campbell in the experimental work as well as Andy Gardea, Jeff Chames and Ryan Nishimoto in metallography and microscopy is gratefully acknowledged. The authors additionally thank Gary Hayden (CP Industries) and John Felbaum (Fiba

Technologies) for providing technologically relevant steels for testing.

APPENDIX A: K-DOMINANCE AT CRACK INITIATION AND CRACK ARREST

K-Dominance at Crack Initiation

For the lower-strength steels in this study, both K_{app} and K_{THa} were relatively high (Figures 3 and 4). As a result, significant plasticity is expected at the crack tip in these lower-strength steels, and the potential implication of this plasticity on the crack-driving forces during the onset of subcritical cracking and at crack arrest must be addressed. Specifically, extensive plasticity can compromise rigorous application of linear-elastic fracture mechanics and the presumption of a highly constrained crack tip.

All values of K_{app} and K_{THa} presented here are calculated using linear-elastic fracture mechanics, however very few of the WOL specimens tested in this study met the specimen size requirements specified by ASTM E1681 for small-scale yielding and plane strain, which requires:

$$B, a, b \geq 2.5 \left(\frac{K_I}{\sigma_0} \right)^2 \quad [A1]$$

where B , a , and b refer to the specimen thickness, crack length, and remaining ligament (W-a), respectively, σ_0 is the yield strength and K_I is the stress-intensity factor. Upon initial loading, only the high-strength SA372 grade L (1053 MPa) specimens met the specimen size criteria, *i.e.*, Eq. [A1] was satisfied with $K_I = K_{app}$ for this steel heat. At crack arrest, the SA372 grade L (1053 MPa) and DOT-3T specimens also met the specimen size criteria, *i.e.*, Eq. [A1] was satisfied with $K_I = K_{THa}$ for these steel heats. None of the other, lower-strength steel specimens satisfied Eq. [A1] at either initial loading or crack arrest. While meeting the specimen size requirements in Eq. [A1] generally ensures plane-strain constraint under small-scale yielding, these conditions are not necessarily compromised in the WOL specimens if Eq. [A1] is not satisfied.

It has been well documented that the specimen size criterion for plane strain is overly conservative for the thickness, B , dimension when appropriate side-grooves are designed into the specimens.^[84] Side-grooves enhance through-thickness constraint, effectively creating plane-strain conditions along the entire crack front, except near the end points where the presence of the free surfaces relaxes the constraint. In the absence of side-grooves, the region of reduced constraint extends further from the surfaces and fracture within this region occurs as 45 deg shear fracture (forming “shear lips”), whereas fracture within the highly constrained, plane-strain region appears flat. When the region of shear fracture contributes to a significant portion of the total crack front, elevated fracture measurements result. However, if the regions of shear fracture are a small fraction of the total crack front, plane-strain fracture can be

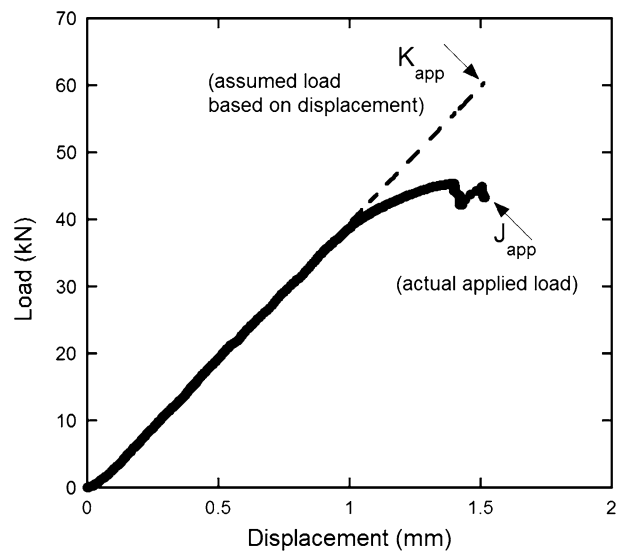


Fig. 10—Load vs crack-opening displacement recorded during initial loading of 4130X WOL specimen. Dashed line shows behavior under linear-elastic loading conditions inherent to the calculation of K_{app} , whereas the solid line shows actual applied load which was used to calculate J_{app} . Fortunately, $K_{app} \sim K_{Japp}$.

assumed.^[84] Shear lips were insignificant along the entire crack length for all WOL specimens tested in this study, suggesting that plane-strain conditions prevailed for all K levels between K_{THa} and K_{app} .

It has been argued that the dimensional requirements for small-scale yielding, *i.e.*, limits on crack length, a , and uncracked ligament, b , in Eq. [A1], were extended to ASTM E1681 and other standards from ASTM E399,^[85] in which these criteria were intended to apply only to the 95 pct secant method for measurement of K_{Ic} . As a result, failure to satisfy the criteria does not necessarily indicate a violation of small-scale yielding.^[86] Rather, it has been suggested that the relative contributions of the elastic and plastic components of the J -integral is a better means to assess small-scale yielding. If the plastic component of J is small relative to the elastic component, then linear-elastic fracture mechanics, *i.e.*, small-scale yielding, is a valid assumption.

The small-scale yielding assumption during initial loading of the WOL specimens was evaluated by estimating J from experimental load vs crack-opening displacement data. Actual load vs displacement data for the 4130X (641 MPa) specimen loaded to the highest value of K_{app} is shown in Figure 10. These data, measured from the load-tup and clip gage during initial loading, reveal deviations from linear behavior. Such deviation from linear behavior was most pronounced for the lower-strength steels loaded to high values of K_{app} and was not observed for the higher-strength steels. In Figure 10, the deviation from linearity is such that the value of load inferred from the final displacement measurement assuming linear-elastic loading is nearly 40 pct higher than the load measured from the load-tup. Based on the load vs displacement data in Figure 10, the plastic component of J was calculated from ASTM E1820 using the relationships for the CT specimen,

which is expected to closely approximate the WOL specimen. The calculations demonstrate that the elastic component of J was 87 kJ/m² and the plastic component was 112 kJ/m².[†] This plastic component is large

[†]This same scenario was also simulated by applying finite element modeling^[20] to the elastic-plastic response of the 4130X (641 MPa) WOL specimen. For the same applied front-face displacement, the total J was calculated as 183 kJ/m², which is within 10 pct of the total J estimated from the experimental load vs displacement data.

relative to the elastic component, suggesting that globally elastic, small-scale yielding behavior is not the case (consistent with the grossly non-linear load vs displacement curve in Figure 10); however, the specimen crack tip is expected to be highly constrained according to the dimensional requirements for plane strain and J -dominance provided by ASTM E1820:

$$b, B \geq 10 \left(\frac{J}{\sigma_0} \right) \quad [\text{A2}]$$

Equation [A2] requires that the thickness, B , and uncracked ligament, b , only equal 3.1 mm, criteria that the WOL specimen easily satisfies. The above analysis was conducted for 4130X specimens, since these tests represented an extreme combination of low yield strength and high K_{app} , and thus exhibited the most severe plastic deformation during loading. In fact, few other specimens exhibited any noticeable deviation from linearity in the measured load vs displacement trace. For the higher-strength steels and those specimens with lower values of K_{app} , the assumption of small-scale yielding during loading is valid.

The lowest-strength steels, *e.g.*, 4130X, do not exhibit small-scale yielding during loading, therefore the relevance of the linear-elastic fracture mechanics quantity K_{app} for characterizing the remote crack-driving force is in question. For those cases in which plasticity caused deviations from linear-elastic loading, the value of K_{app} calculated from the front-face displacement assuming linear-elastic behavior (*e.g.*, 199 MPa $\sqrt{\text{m}}$ for 4130X) is fortuitously a good representation of the elastic-plastic loading condition, since K_{Japp} equals 212 MPa $\sqrt{\text{m}}$ (calculated from the $J_{\text{app}} = 183 \text{ kJ/m}^2$ determined above using experimental load vs displacement data); *i.e.*, $K_{\text{app}} \approx K_{\text{Japp}}$. Therefore, it appears that K_{app} calculated using the linear-elastic fracture mechanics relationship in Eq. [1] provides an approximate representation of remote crack-driving force for the entire range of elastic-plastic behavior exhibited by the specimens in this study. It must be noted that this result is not a general conclusion, and the coincidence of K_{app} and K_{Japp} must be verified before assuming that it applies to lower-strength steels or to different specimen geometries.

K-Dominance at Crack Arrest

As described in Section III-A, subcritical cracking progressed through a large fraction of the specimen

width in most WOL specimens, such that the final crack length-to-width (a/W) ratio of the arrested crack was typically greater than 0.8. Consequently, the presumption that the linear-elastic stress-intensity factor, K , uniquely characterized the crack-tip stress and strain fields at crack arrest was in question. Whereas the extent of crack-tip plasticity during loading of the WOL specimens could be assessed using experimental load vs displacement data to estimate the relative plastic and elastic contribution to the J -integral, a similar evaluation at crack arrest required numerical simulation since unloading which occurs as the cracks propagate violates the proportional loading assumption that underlies the validity of the J -integral. The finite element method was used to assess K -dominance at the arrested crack tip.

To address this issue, numerical calculations were conducted using Abaqus Standard^[87] to demonstrate that K governed the crack-tip fields in WOL specimens that represented the experiments. Finite strain elastoplastic deformation was implemented in the simulations. In the elastic regime, the material was assumed to be linear and isotropic and in the plastic regime to obey normality, with von Mises yielding and isotropic hardening. Data from uniaxial tension tests (provided by the material supplier) were used to construct the flow stress as a function of plastic strain. The WOL specimen was discretized with eight-noded isoparametric plane-strain elements. Deep cracks ($a/W = 0.81$ and 0.94) were loaded to crack-mouth-opening displacements comparable to those used in the experiments. It is noted that contour plots of the effective plastic strain in the neighborhood of the crack tip can be used to discern whether plasticity is confined to the crack tip. Two approaches for evaluating K -dominance were considered, each of which assessed the condition of an arrested crack near the back face of the specimen. The effect of crack propagation history on the crack-tip fields was not considered.

The first approach to assess K -dominance was to evaluate the extent of plasticity through calculations of the J -integral. The domain integral approach on contours around the crack tip was utilized to calculate the value of the J -integral. The associated stress-intensity factor can be determined from

$$K_J = \sqrt{\frac{EJ}{1 - \nu^2}} \quad [\text{A3}]$$

The criterion for K -dominance is based on comparing this value of K_J to the stress-intensity factor calculated numerically for the WOL specimen under the assumption of purely elastic specimen response.

The second approach to assess K -dominance was to compare the stress profiles as calculated ahead of the blunting crack tip in the full-field simulation of the WOL specimen with those prevailing at the crack tip under small-scale yielding (SSY) conditions. The SSY domain was loaded under plane strain by remote displacements associated with the stress-intensity factor K_I obtained from the elastic analysis of the WOL specimen. Thus, the asymptotic displacements of the

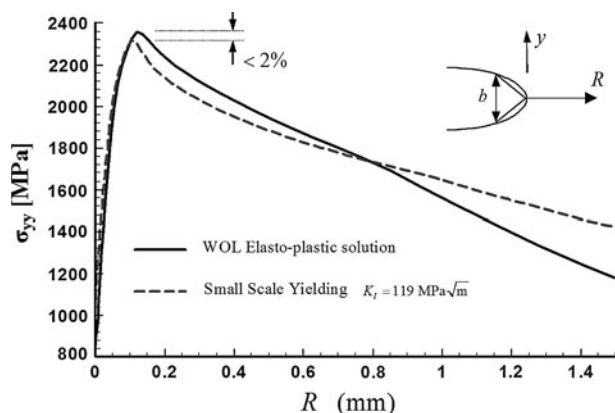


Fig. 11—Comparison of the crack-tip opening stress, σ_{yy} , on the plane of symmetry ahead of the crack in the WOL specimen with the small-scale yielding solution. Flow properties representative of the SA372 grade J (717 MPa) steel were used. The simulation for the WOL specimen was done with the specimen loaded to a crack-opening displacement $V_{FF} = 1.26$ mm and the crack tip positioned at $a/W = 0.81$.

Irwin singular linear elastic field^[88] were prescribed remotely from the crack tip. These displacements were imposed incrementally at a constant stress-intensity factor rate toward the final value of K_I , which was selected to be consistent with experimentally measured values of K_{THa} .

Full-field simulations of the crack-tip stresses and strains were conducted by modeling a WOL specimen of SA372 grade J (717 MPa) having a stationary crack at $a/W = 0.81$. The front-face displacement was $V_{FF} = 1.26$ mm which resulted in $K_{THa} = 109$ MPa \sqrt{m} (as determined using Eq. [1]); these values directly replicate measurements from one of the specimens in the experimental study. The elastic finite element analysis gave $K = 119$ MPa \sqrt{m} , while K_I from elastic-plastic analysis was 116 MPa \sqrt{m} . The similarity of the calculated K and K_I values indicates that small-scale yielding prevailed. In addition to comparing these remote-loading parameters, Figure 11 shows the crack-opening stress, σ_{yy} , along the axis of symmetry ahead of the crack tip for the representative WOL specimen from SA372 grade J. Superposed on the same figure is the opening stress as furnished by the SSY solution. The strong agreement between these two solutions confirms that there is K -dominance at crack arrest. In summary, the FEM analysis suggests that K_I accurately describes the crack-tip fields even at these long final crack lengths near the back face of the specimen. This conclusion is consistent with the comparison of results from experiments on straight-notched and chevron-notched WOL specimens, in which K_{THa} was not dependent on a/W .

REFERENCES

1. R.P. Gangloff, in *Comprehensive Structural Integrity*, I. Milne, R.O. Ritchie, and B. Karimhaloo, eds., Elsevier Science, New York, NY, 2003, pp. 31–101.
2. A.W. Thompson and I.M. Bernstein: in *Advances in Corrosion Science and Technology*, vol. 7: *Hydrogen-Assisted Environmental*

Fracture, M.G. Fontana, R.W. Staehle, eds., Plenum Publishing Corporation, New York, 1980, pp. 53–175.

3. H.K. Birnbaum, I.M. Robertson, P. Sofronis and D. Teter: *Proceedings of the Second International Conference on Corrosion-Deformation Interactions, CDI 96*, T. Magnin ed., Woodhead Publishing Limited, Cambridge, 1997.
4. I.M. Bernstein: *Mater. Sci. Eng.*, 1970, vol. 6, pp. 1–19.
5. J.P. Hirth: *Metall. Trans. A*, 1980, vol. 11A, pp. 861–90.
6. R.A. Oriani: *Annu. Rev. Mater. Sci.*, 1978, vol. 8, pp. 327–57.
7. H.G. Nelson: *Hydrogen Embrittlement Testing, ASTM STP 543*, ASTM, Philadelphia, PA, 1974, pp. 152–69.
8. P. McIntyre: *Hydrogen Degradation in High Strength Steels*, R.A. Oriani, J.P. Hirth and M. Smialowski, eds., Noyes Publications, New Jersey, 1985, pp. 763–98.
9. A.W. Loginow and E.H. Phelps: *Corrosion*, 1975, vol. 31, pp. 404–12.
10. M. Dadfarnia, P. Sofronis, B.P. Somerday, D.K. Balch, P. Schembri, and R. Melcher: *Eng. Fract. Mech.*, 2011, vol. 78, pp. 2429–38.
11. W.G. Clark and J.D. Landes: *Stress Corrosion—New Approaches, ASTM STP 610*, ASTM, Philadelphia, PA, 1976, pp. 108–27.
12. R.P. Gangloff: *Hydrogen Effects on Materials Behavior and Corrosion Deformation Interactions*, N.R. Moody, A.W. Thompson, R.E. Ricker, G.W. Was, and R.H. Jones, eds., The Minerals Metals and Materials Society, Warrendale, PA, 2003, pp. 477–97.
13. ASTM E1681-03, *Annual Book of ASTM Standards*, ASTM International, West Conshohocken, PA, 2003.
14. R.P. Wei and S.R. Novak: *J. Test. Eval.*, 1987, vol. 15, pp. 38–75.
15. J.H. Underwood, W.A. Van Der Sluys, and G.N. Vigilante: *Technical Report ARCCB-TR-97016*, US Army Armament Research, Development and Engineering Center, Benet Laboratories, Watervliet, NY, 1997.
16. G.N. Vigilante, J.H. Underwood, D. Crayon, S. Tauscher, T. Sage and E. Troiano: *Fatigue and Fracture: 28th Volume, ASTM STP 1321*, J.H. Underwood, B.D. Macdonald and M.R. Mitchell, eds., ASTM, West Conshohocken, PA, 1997, pp. 602–16.
17. H.P. Seifert and S. Ritter: *J. Nucl. Mater.*, 2008, vol. 372, pp. 114–31.
18. J. Heldt and H.P. Seifert: *Nucl. Eng. Des.*, 2001, vol. 206, pp. 57–89.
19. EIGA Doc 100/03/E: *Hydrogen Cylinders and Transport Vessels*, European Industrial Gases Association, Brussels, Belgium, 2003.
20. K.A. Nibur, B.P. Somerday, C. San Marchi, J.W. Foulk, III, M. Dadfarnia, P. Sofronis, and G.A. Hayden: *Sandia Report SAND2010-4633*, Sandia National Laboratories, Livermore, CA, 2010.
21. W.J. Drugan, J.R. Rice, and T.-L. Sham: *J. Mech. Phys. Solids*, 1982, vol. 30, pp. 447–73.
22. M.R. Begley, J.A. Begley and C.M. Landis: *Gaseous Hydrogen Embrittlement of Materials in Energy Technologies Volume 2: Mechanics, Modelling and Future Developments*, R.P. Gangloff and B.P. Somerday, eds., Woodhead Publishing Limited, Cambridge, UK, 2011, pp. 286–325.
23. B.P. Somerday, L.M. Young, and R.P. Gangloff: *Fatigue Fract. Eng. Mater. Struct.*, 2000, vol. 23, pp. 39–58.
24. M.M. Hall, Jr.: *Corros. Sci.*, 2008, vol. 50, pp. 2902–05.
25. W.W. Gerberich and S. Chen: *Environment-Induced Cracking of Metals: Proceedings of the First International Conference on Environment-Induced Cracking of Metals*, R.P. Gangloff and M.B. Ives, eds., NACE, Houston TX, 1988, pp. 167–87.
26. S.H. Chen, Y. Katz, and W.W. Gerberich: *Philos. Mag. A*, 1991, vol. 63, pp. 131–55.
27. M.W. Perra: *Environmental Degradation of Engineering Materials in Hydrogen*, M.R. Louthan, R.P. McNitt, and R.D. Sisson, eds., VPI Press, Blacksburg, VA, 1981 pp. 321–33.
28. ASTM E1820-09: *Annual Book of ASTM Standards*, ASTM International, West Conshohocken, PA, 2009.
29. ASTM E1737-96: *Annual Book of ASTM Standards*, ASTM International, West Conshohocken, PA, 1996.
30. R.L.S. Thomas, J.R. Scully, and R.P. Gangloff: *Metall. Trans. A*, 2003, vol. 34A, pp. 327–44.
31. R. Zawierucha and K. Xu: *Proceedings of Materials Science, Technology 2005: Materials for the Hydrogen Economy*, TMS, Warrendale, PA, 2005, pp. 79–90.
32. C. San Marchi, B.P. Somerday, K.A. Nibur, D.G. Stalheim, T. Boggess, and S. Jansto: *Proceedings of the ASME 2010 Pressure*

- Vessels and Piping Division/K-PVP Conference, PVP2010-25825*, ASME, New York, NY, 2010.
33. Y. Takeda and C.J. McMahon, Jr.: *Metall. Trans. A*, 1981, vol. 12A, pp. 1255–66.
 34. J.E. Costa and A.W. Thompson: *Metall. Trans. A*, 1981, vol. 12A, pp. 761–71.
 35. M. Gao, M. Lu, and R.P. Wei: *Metall. Trans. A*, 1984, vol. 15A, pp. 735–46.
 36. T.D. Lee, T. Goldenberg, and J.P. Hirth: *Metall. Trans. A*, 1979, vol. 10A, pp. 199–208.
 37. C.D. Beachem: *J. Basic Eng. (Trans. ASME Series D)*, 1965, vol. 87, pp. 299–306.
 38. H.C. Burghard, Jr. and N.S. Stoloff: *Electron Fractography, ASTM STP 436*, ASTM, Philadelphia, PA, 1968, pp. 32–58.
 39. A.W. Thompson: *Fatigue Fract. Mater. Struct.*, 1996, vol. 19, pp. 1307–16.
 40. C.D. Beachem and R.M.N. Pelloux: *Fracture Toughness Testing and its Applications, STP 381*, ASTM, Philadelphia, PA, 1965, pp. 210–244.
 41. *Electron Fractography: ASTM STP 436*, C.D. Beachem, ed., ASTM International, Philadelphia, PA, 1967.
 42. M.L. Martin, J.A. Fenske, G.S. Liu, P. Sofronis, and I.M. Robertson: *Acta Mater.*, 2011, vol. 59, pp. 1601–06.
 43. M.R. Bache, W.J. Evans, and H.M. Davies: *J. Mater. Sci.*, 1997, vol. 32, pp. 3435–42.
 44. M.Q. Jiang, Z. Ling, J.X. Meng, and L.H. Dai: *Philos. Mag.*, 2008, vol. 88, pp. 407–26.
 45. K. Tokaji, M. Kamakura, Y. Ishiizumi, and N. Hasegawa: *Int. J. Fatigue*, 2004, vol. 26, pp. 1217–24.
 46. C.J. McMahon, Jr.: *Hydrogen Effects in Metals*, I.M. Bernstein and A.W. Thompson, eds., The Metallurgical Society of AIME, Warrendale, PA, 1981, pp. 219–34.
 47. F. Nakasato and I.M. Bernstein: *Metall. Trans. A*, 1978, vol. 9A, pp. 1317–1326.
 48. A.W. Thompson and I.M. Bernstein: *Advances in Research on the Strength and Fracture of Materials, Vol. 2A, Proceedings of the Fourth International Conference on Fracture*, D.M.R. Taplin, ed., Pergamon Press, Oxford, 1977, pp. 249–54.
 49. M.L. Martin, I.M. Robertson, and P. Sofronis: *Acta Mater.*, 2011, vol. 59, pp. 3680–87.
 50. D. Kwon and R.J. Asaro: *Metall. Trans. A*, 1990, vol. 21A, pp. 117–134.
 51. I.M. Robertson: *Eng. Fract. Mech.*, 1999, vol. 64, pp. 649–73.
 52. I.M. Robertson, M.L. Martin, and J.A. Fenske: *Gaseous Hydrogen Embrittlement of Materials in Energy Technologies*, R.P. Gangloff and B.P. Somerday, eds., Woodhead Publishing Limited, Cambridge, UK, 2011, pp. 166–206.
 53. K.A. Nibur, D.F. Bahr, and B.P. Somerday: *Acta Mater.*, 2006, vol. 54, pp. 2677–84.
 54. K.A. Nibur, B.P. Somerday, D.K. Balch, and C. San Marchi: *Acta Mater.*, 2009, vol. 57, pp. 3795–09.
 55. H.E. Hanninen, T.C. Lee, I.M. Robertson, and H.K. Birnbaum: *J. Mater. Eng. Perform.*, 1993, vol. 2, pp. 807–17.
 56. R.O. Ritchie and A.W. Thompson: *Metall. Trans. A*, 1985, vol. 16A, pp. 233–48.
 57. R.H. Dean and J.W. Hutchinson: *Fracture Mechanics: Twelfth Conference, ASTM STP 700*, American Society for Testing and Materials, West Conshohocken, PA, 1980, pp. 383–405.
 58. J.R. Rice and E.P. Sorensen: *J. Mech. Phys. Solids*, 1978, vol. 26, pp. 163–86.
 59. O.A. Onyewuenyi and J.P. Hirth: *Metall. Trans. A*, 1983, vol. 14A, pp. 259–69.
 60. N.F. Mott and F.R.N. Nabarro: *Physical Society Bristol Conference Report*, 1948, pp. 1–19.
 61. A.H. Cottrell: *Philos. Mag. Lett.*, 2002, vol. 82, pp. 65–70.
 62. M.M. Hall, Jr.: *Report CONF-9505335-1, Alloy 600 Experts Meeting sponsored by the Electric Power Research Institute*, Electric Power Research Institute, 1993.
 63. S. Wang, Y. Zhang, and W. Chen: *J. Mater. Sci.*, 2001, vol. 36, pp. 1931–38.
 64. C.G. Park, K.S. Shin, J. Nagakawa, and M. Meshii: *Scripta Metall.*, 1980, vol. 14, pp. 279–84.
 65. A. Barnoush, M. Zamanzade, and H. Vehoff: *Scripta Metall.*, 2010, vol. 62, pp. 242–45.
 66. H.K. Birnbaum and P. Sofronis: *Mater. Sci. Eng.*, 1994, vol. A176, pp. 191–202.
 67. E. Sirois and H.K. Birnbaum: *Acta Metall. Mater.*, 1992, vol. 40, pp. 1437–85.
 68. R.M. Rieck, A. Atrens, and I.O. Smith: *Metall. Trans. A*, 1989, vol. 20A, pp. 889–895.
 69. A. Oehlert and A. Atrens: *Acta Metall. Mater.*, 1994, vol. 42, pp. 1493–08.
 70. R.N. Parkins: *Stress Corrosion Cracking – The Slow Strain-Rate Technique, ASTM STP 665*, G.M. Ugiansky and J.H. Payer, eds., ASTM, Philadelphia, PA, 1979, pp. 5–25.
 71. K.A. Nibur, B.P. Somerday, C. SanMarchi and D.K. Balch: *Proceedings of 2008 ASME Pressure Vessels and Piping Division Conference, PVP2008-61298*, 2008.
 72. V. Vitek: *Int. J. Fract.*, 1977, vol. 13, pp. 481–501.
 73. J.W. Hutchinson: *J. Mech. Phys. Solids*, 1968, vol. 16, pp. 13–31.
 74. J.R. Rice and G.F. Rosengren: *J. Mech. Phys. Solids*, 1968, vol. 16, pp. 1–12.
 75. R.O. Ritchie, W.L. Server, and R.A. Wullaert: *Metall. Trans. A*, 1979, vol. 10A, pp. 1557–1570.
 76. J.R. Rice: *Fracture: an Advanced Treatise – Vol. 2: Mathematical Fundamentals*, H. Liebowitz, ed., Academic Press, 1968, Chapter 3, pp. 191–311.
 77. F.A. McClintock and G.R. Irwin: *Fracture Toughness Testing and its Applications, ASTM STP 381*, American Society for Testing and Materials, Chicago, 1965, pp. 84–113.
 78. J.R. Rice, W.J. Drugan, and T.-L. Sham: *Fracture Mechanics: Twelfth Conference, ASTM STP 700*, American Society for Testing and Materials, Philadelphia, PA, 1980, pp. 189–221.
 79. J.R. Rice: *Mechanics of Solids: The Rodney Hill 60th Anniversary Volume*, H.G. Hopkins and M.J. Sewell, eds., Pergamon Press, Oxford, England, 1982, pp. 539–62.
 80. K.S. Chan: *Metall. Trans. A*, 1990, vol. 21A, pp. 69–80.
 81. W.W. Gerberich, D.L. Davidson, and M. Kaczorowski: *J. Mech. Phys. Solids*, 1990, vol. 38, pp. 87–113.
 82. Y.-C. Gao and K.-C. Hwang: *Advances in Fracture Research: Proceedings of the Fifth International Conference on Fracture*, U.K., 1982, pp. 669–82.
 83. R. Irani: *Hydrogen Embrittlement: How It Was Resolved in the 1980's*, Presentation from ISO TC58/WG7, Gas Cylinder Compatibility, Atlanta GA, 29 Sept. 2008.
 84. T.L. Anderson: *Fracture Mechanics Fundamentals and Applications*, 3rd ed., Taylor and Francis, Boca Raton FL, 2005.
 85. ASTM E399-06: *Annual Book of ASTM Standards*, ASTM International, West Conshohocken, PA, 2006.
 86. J.A. Joyce and R.L. Tregoning: *Fatigue, Fracture Mechanics: 30th Volume, ASTM STP 1360*, ASTM, West Conshohocken, PA, 2000, pp. 357–376.
 87. HKS: *Abaqus Version 6.7, Theory Manual*. Hibbit, Karlsson, and Sorensen, Providence, RI, 2007.
 88. G.R. Irwin: *Structural Mechanics, Proceedings of the First Symposium of Naval Structural Mechanics*, J.N. Goodier and N.J. Hoff, eds., Pergamon Press, Oxford, 1960, pp. 557–94.